Hydrol. Earth Syst. Sci., 28, 2661–2682, 2024
https://doi.org/10.5194/hess-28-2661-2024
© Author(s) 2024. This work is distributed under
the Creative Commons Attribution 4.0 License.

Hydrology and Earth System Sciences
Open Access

A comprehensive framework for stochastic calibration and sensitivity analysis of large-scale groundwater models

Andrea Manzoni, Giovanni Michele Porta, Laura Guadagnini, Alberto Guadagnini, and Monica Riva

Dipartimento di Ingegneria Civile e Ambientale (DICA), Politecnico di Milano, 20133 Milano, Italy

Correspondence: Monica Riva (monica.riva@polimi.it)

Received: 10 November 2023 – Discussion started: 11 December 2023
Revised: 12 March 2024 – Accepted: 22 April 2024 – Published: 25 June 2024

Abstract. We introduce a comprehensive and robust theoretical framework and operational workflow that can be employed to enhance our understanding, modeling and management capability of complex heterogeneous large-scale groundwater systems. Our framework encapsulates key components such as the three-dimensional nature of groundwater flows, river–aquifer interactions, probabilistic reconstruction of three-dimensional spatial distributions of geomaterials and associated properties across the subsurface, multi-objective optimization for model parameter estimation through stochastic calibration, and informed global sensitivity analysis (GSA). By integrating these components, we effectively consider the inherent uncertainty associated with subsurface system characterizations as well as their interactions with surface waterbodies. The approach enables us to identify parameters impacting diverse system responses. By employing a coevolutionary optimization algorithm, we ensure efficient model parameterization, facilitating simultaneous and informed optimization of the defined objective functions. Additionally, estimation of parameter uncertainty naturally leads to quantification of uncertainty in system responses. The methodology is designed to increase our knowledge of the dynamics of large-scale groundwater systems. It also has the potential to guide future data acquisition campaigns through an informed global sensitivity analysis. We demonstrate the effectiveness of our proposed methodology by applying it to the largest groundwater system in Italy. We address the challenges posed by the characterization of the heterogeneous spatial distribution of subsurface attributes across large-scale three-dimensional domains upon incorporating a recent probabilistic hydrogeological reconstruction specific to the study case. The system considered faces multiple challenges, including groundwater contamination, seawater intrusion, and water scarcity. Our study offers a promising modeling strategy applicable to large-scale subsurface systems and valuable insights into groundwater flow patterns that can then inform effective system management.

1 Introduction

Large-scale groundwater flow models have been developed in recent years (e.g., Maxwell et al., 2015; Naz et al., 2023) in response to growing interest in understanding potential impacts of climate and anthropogenic drivers on water systems as well as in assessing large-scale patterns and processes affecting water security. This progress has been facilitated by an increased availability of data and computational capabilities (e.g., Zhou and Li, 2011; Amanambu et al., 2020, and references therein). Building such large-scale models often requires consideration of important simplifications. In some cases, constant properties are assumed along the vertical direction (e.g., Maxwell et al., 2015; Shrestha et al., 2014; Soltani et al., 2022), without taking into account the three-dimensional nature of the spatial heterogeneity of the subsurface system. In addition, parameterization of these models does not rely on rigorous model calibration against data that are, in turn, typically scarce. Instead, parameter values are typically inferred from literature information (Naz et al., 2023; Maxwell et al., 2015), thus possibly introducing large margins of uncertainty that are seldom quantifiable. The work of Manzoni et al. (2023) addresses these challenges by proposing a machine-learning-based methodology for delineating the spatial distribution of geomaterials across large-scale three-dimensional subsurface systems. These authors showcase their approach upon focus-

ing on the Po River basin in northern Italy. Their work provides a comprehensive dataset comprising lithostratigraphic data from various sources and offers a robust framework for quantifying prediction uncertainty at each spatial location within the reconstructed domain. Hence, our study rests on the findings of Manzoni et al. (2023). In this sense, the latter serves as more than simply a dataset but as a critical component upon which we build our groundwater flow model calibration. Although the literature includes examples of large-scale and national-scale models covering extensive areas ($\sim 10\,000\,\mathrm{km}^2$; e.g., Sophocleous and Perkins, 2000; De Lange et al., 2014; Højberg et al., 2013), these models are calibrated only across specific portions of the system, thus challenging their predictive capabilities. Even in these cases, uncertainty associated with the estimated model parameters is usually overlooked. De Graaf et al. (2020) present a detailed geological reconstruction for the same domain analyzed by Maxwell et al. (2015). Due to computational constraints, their model could only simulate groundwater flow within selected portions of the domain and calibration of model parameters for the entire model domain was not achieved. Recently, Mather et al. (2022) introduced a three-dimensional data-driven model of continental-scale groundwater flow. It is noted that data-driven models are heavily constrained by the quantity and quality of available training data. In this context, groundwater flow and pressure data may not be as readily accessible as, for example, lithostratigraphic data (see, e.g., Manzoni et al., 2023) across the entire domain, especially when considering large-scale scenarios. In general, a comprehensive calibration strategy encompassing the entire geographical extent of the model domain is still lacking.

Groundwater systems are inherently heterogeneous, thus rendering modeling of flow and transport processes in such complex domains prone to uncertainty. The latter stems from the (generally unknown) spatial distribution of medium properties, boundary conditions and/or forcing terms, and limited data availability. This issue could be addressed upon relying on a stochastic framework for model calibration (e.g., Neuman, 2003; Riva et al., 2009; Ye et al., 2010; Panzeri et al., 2015; Siena and Riva, 2020). However, stochastic model calibration presents significant challenges, particularly in terms of computational cost when dealing with multiple sources of uncertainty (e.g., Vrugt et al., 2008; Hendricks Franssen et al., 2009; Zhou et al., 2014). Although stochastic model calibration has become feasible at laboratory scales ($\sim 10^{-2}$–$1\,\mathrm{m}^2$) and at experimental sites of limited areal extent (~ 1–$100\,\mathrm{km}^2$), the impact on the hydraulic response across large-scale fields stemming from the inherent uncertainty plaguing our knowledge of the subsurface is still largely unexplored. In this framework, Bianchi Janetti et al. (2019, 2021) analyze how the uncertainty related to the characterization of the subsurface system affects the distribution of hydraulic heads and subsurface fluxes in a regional-scale hydrological setting ($\sim 1000\,\mathrm{km}^2$).

Here, we introduce and test a methodological approach for stochastic model calibration tailored to large-scale scenarios (exceeding $10\,000\,\mathrm{km}^2$). Our proposed methodology combines a suite of tools that have not been previously employed to address groundwater modeling at such a vast scale and with such a level of system complexity. These include (a) modeling the dynamics of groundwater flow across a three-dimensional setting, (b) embedding and analyzing interactions between rivers and aquifers in detail, (c) relying on a probabilistic reconstruction of geological material distributions and attributes, (d) resting on multi-objective optimization techniques for stochastic calibration of large-scale groundwater models, and (e) performing a detailed informed global sensitivity analysis to assess the degree of spatial variability and the relative importance of uncertain model parameters therein. Through incorporation of these tools, our methodological and operational workflow yields a calibrated model that enhances our understanding of aquifer dynamics from a holistic perspective. It also reveals insights into the spatial pattern of the sensitivity of model outputs to model parameters. Results associated with the latter element can be employed to inform future data acquisition efforts to improve model parameterization and hydraulic head estimates. They also emphasize the need to balance model complexity with simplifications that might be required to tackle large-scale groundwater scenarios. The approach involves the development of a groundwater model that includes a probabilistic three-dimensional hydrogeological reconstruction of the investigated area. As stated above, we do so upon integrating the results illustrated by Manzoni et al. (2023). Specifically, we leverage their probabilistic three-dimensional hydrogeological reconstruction, which enables us to infer the spatial distribution of geological properties at a scale that was previously unattainable. By incorporating this advanced hydrogeological reconstruction into our workflow, we address key challenges posed by uncertainties that are inherent to large-scale groundwater systems. Multi-objective optimization is a key step in assessing the way model parameters impact diverse system responses. This challenge is addressed by relying on a coevolutionary optimization framework that is applied to a differential evolution optimization algorithm, thus ensuring effective control over the optimization process while preserving computational efficiency (e.g., Dagdia and Mirchev, 2020; Trunfio, 2015). The resulting algorithm is designed to handle multiple objectives and eliminates the need to assess their relative weights within the overall objective function (Khan et al., 2022). The methodology we present is designed to not only increase our knowledge about the dynamics of large-scale systems but also guide future data acquisition campaigns. The latter goal is attained by making use of an informed global sensitivity analysis (GSA). We recall that GSA typically serves as a tool to assess the relative impact of uncertain model inputs on model outputs of interest (Morris, 1991; Campolongo et al., 2007; Razavi and Gupta, 2015; Pianosi et al., 2016; Dell'Oca et al., 2017).

An informed GSA (Dell'Oca et al., 2020) is performed after (stochastic) model calibration and enables one to quantify the influence of residual (i.e., following model calibration) uncertainty associated with model parameter estimates on predictions of system dynamics. This strategy aligns with our focus on tackling major challenges posed by large-scale subsurface flow scenarios. It offers critical insights into model functioning through quantification of the impact of model parameters on target model outputs. It also provides guidance on the identification of locations where acquiring additional information can enhance the accuracy of parameter estimates and ultimately constrain the uncertainty associated with model results.

The proposed methodological approach is then employed to analyze the largest groundwater system in Italy, which corresponds to the Po River watershed. This region faces a variety of challenges related to groundwater contamination (Guadagnini et al., 2020; Balestrini et al., 2021), seawater intrusion (Colombani et al., 2016), and water scarcity (Bozzola and Swanson, 2014). Thus, the design of comprehensive policies addressing risks to water quality across large-scale groundwater systems of this kind is grounded on the implementation of a modeling framework capable of addressing the key patterns of groundwater flow at the scale of the entire domain (Giuliano, 1995; Nespoli et al., 2021).

The work is organized as follows. Section 2 provides an overview of the large-scale groundwater system we consider. The proposed methodology and workflow are illustrated in Sect. 3. Section 3.1 describes the modeling approach employed to assess groundwater recharge. Section 3.2 focuses on the large-scale groundwater model, which involves integrating data from multiple sources, such as large-scale hydrogeological reconstruction, remote sensing, and global-scale databases. Section 3.3 delves into the inverse modeling approach employed and introduces a novel application of a coevolutionary algorithm to address the multi-objective function associated with large-scale hydrogeology settings. Section 3.4 describes the informed GSA approach. Key results are presented in Sect. 4, while Sect. 5 summarizes main findings and implications.

2 General setting

Our analysis focuses on the Po River basin. Along with the Rhône and the Nile, the Po is one of the main Mediterranean rivers. With an average flow rate of about $1500\,m^3\,s^{-1}$, the Po River has more than 140 tributaries, forming an intricate network of waterways that also intersects with a dense network of irrigation canals (ISPRA, 2010). This area (denoted as Po Plain, Pianura Padana) encompasses the largest and most exploited groundwater system across Italy, which provides fresh water to about 24 million residents (ISTAT, 2020). This area holds significant economic importance, contributing nearly 40 % of Italy's gross domestic product. Due to the high density of industrial and agricultural activities, the system is facing a significant risk of overexploitation and possible exposure to multiple contaminants (AdB-Po, 2021). Seawater intrusion is also a potential negative issue in the coastal portion of the system (Kazakis et al., 2019; Antonellini et al., 2008).

As shown in Fig. 1, the domain is geographically bounded by the Adige River to the northeast and by the Adriatic Sea to the east, while its remaining boundaries coincide with the mountain ranges of the Alps and the Apennines.

Our study is framed across the entire Po River district (AdB-Po, 2021). The latter covers approximately $87\,000\,km^2$, spanning nine Italian regions as well as the Swiss canton of Ticino and some valleys in the French and Swiss Alps (see Fig. 1). This area includes the entire catchment area of the Po River ($\sim 72\,000\,km^2$). The main features of the study area vary from the high peaks of the Alps and Apennines (with altitude exceeding 4000 m above sea level, steep slopes of more than 15 %, and a population density of less than 1 inhabitant per km^2) to flat terrain and densely populated areas (with more than 2000 inhabitants per km^2) (SEDAC, 2018). The district also experiences notable climatic differences. The lowland area is characterized by a continental and temperate climate with moderate annual precipitation levels ranging from 600 to 900 mm (Morgan, 1973; Grimm et al., 2023). The Alps include a variety of climate zones at different elevations, corresponding to distinct biotic features. These zones are often characterized by multiple precipitation patterns, including both snow and rain (Elsasser and Bürki, 2002; Agrawala, 2007). The foothill (Prealpi) zone features highest cumulative precipitation levels, with an annual precipitation of 1500–2000 mm (Fratianni and Acquaotta, 2017; Morgan, 1973).

3 Methods

Steady-state groundwater flow across the large-scale system described in Sect. 2 is evaluated through a three-dimensional finite-element model that we develop in the OpenGeoSys v. 6.4.1 (Bilke et al., 2022). We describe the methodology used for evaluating groundwater recharge in Sect. 3.1. This step is performed within the entire Po district (i.e., not only within the considered groundwater system) to assess (i) surface recharge within the domain and (ii) contributions of the surrounding basins to lateral flow exchanges with the domain. Section 3.2, 3.3, and 3.4 include key details about the groundwater model, its calibration, and the informed GSA, respectively. Figure 2 illustrates the conceptual workflow of the proposed methodology.

3.1 Groundwater recharge

We estimate the spatial and temporal variations in groundwater recharge at the scale of the entire Po district

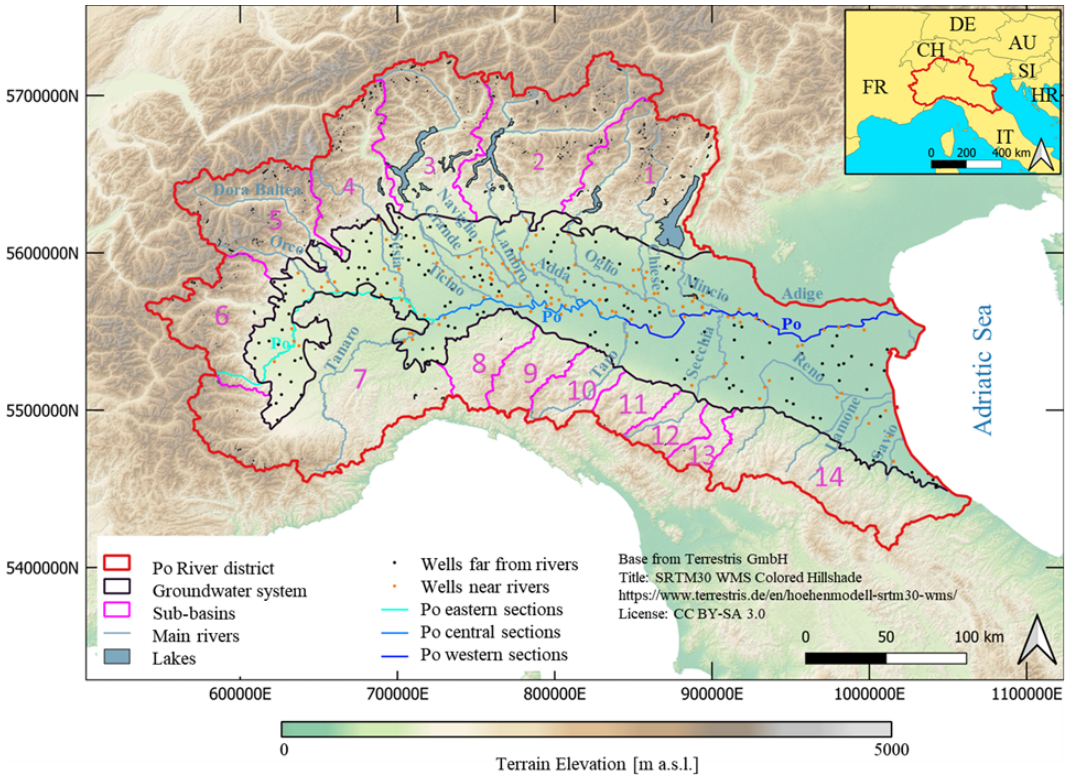

Figure 1. Spatial location of the Po River district, including the Po Plain groundwater system and the sub-basins considered to assess lateral flow boundary conditions. Dots correspond to locations of wells for which head data are available. The coordinate reference system (CRS) is ESRI:54012.

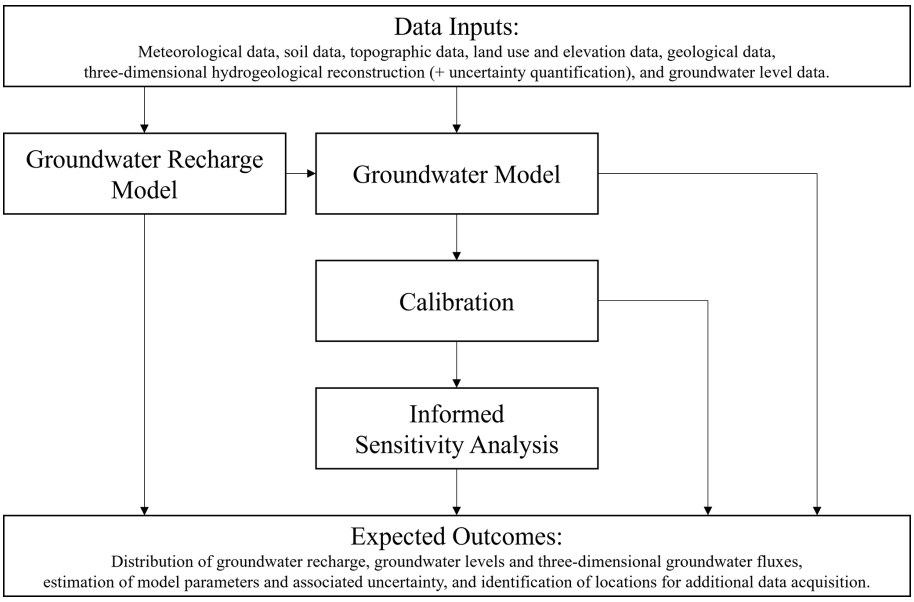

Figure 2. Conceptual workflow for stochastic calibration and informed global sensitivity analysis of large-scale groundwater models.

($\sim 87\,000\,\mathrm{km}^2$). The study area is discretized into square cells with a spatial resolution of 250×250 m (resulting in approximately 1.4 million cells). Cell elevation data are obtained through the European Digital Elevation Model (ESA, 2019).

Groundwater recharge, R, is evaluated within each grid cell upon making use of the soil water balance method of Thornthwaite (1948) and Thornthwaite and Mather (1955, 1957), as implemented in the widely used and tested (e.g., Zhang et al., 2016; Shuler et al., 2021; Roland et al., 2021) USGS SWB model version 2.0 (Westenbroek et al., 2018), i.e.,

$$R = \mathrm{RG} + \mathrm{SM} + \mathrm{IRR} + R_{\mathrm{in}} - \mathrm{ET} - R_{\mathrm{off}} - (\mathrm{SWHC} - \mathrm{SWC}) \,. \quad (1)$$

Here, RG is the non-intercepted rain (rainfall reaching the ground); SM is snowmelt; IRR is irrigation; ET is actual evapotranspiration; and R_{in} and R_{off} are overland inflow and outflow, respectively. The last term in Eq. (1) corresponds to the amount of water that can still be stored in the soil at a given time, SWHC and SWC being soil water holding capacity and soil water content, respectively. Equation (1) is solved with a temporal resolution equal to 1 d, covering the entire period from January 2010 to December 2019. Due to uncertainty in initial conditions, model results from January 2010 to December 2012 are discarded as they are associated with the warm-up periods of the hydrological model (see, e.g., Kim et al., 2018).

Meteorological data (such as precipitation and temperature) are obtained from the latest generation of ECMWF reanalysis data from ERA5 (Muñoz-Sabater et al., 2021). This dataset includes daily maximum and minimum temperatures evaluated at an elevation of 2 m above ground as well as precipitation data. The spatial distribution of the required soil information is collected from the global-scale maps of Poggio et al. (2021). To estimate the land cover type, we integrate crop type spatial distribution data from the EU crop map (d'Andrimont et al., 2021) into the CORINE land cover map (European Environment Agency, 2018).

For the evaluation of RG, we account for a water interception budget. The latter represents the amount of precipitation that can be intercepted by vegetation. This interception budget varies across space depending on land use. Precipitation must exceed the intercepted amount in order to reach the soil and contribute to the soil water balance. The accumulation and melting term, SM, is evaluated on the basis of precipitation and maximum and minimum daily temperatures, as proposed by Dripps and Bradbury (2007). We recall that, according to previous studies (Farinotti et al., 2016), the investigated area receives a significant contribution from glacier melt. The irrigation term, IRR, is triggered only in the absence of precipitation during a crop-specific irrigation period. It is evaluated (in each cell) by dividing the crop water need (i.e., the amount of water required to meet the evapotranspiration losses considering the crop type and its growth stage) by the field application efficiency. We rely on the FAO-56 model (Allen et al., 1998) to assess the crop water need for 31 diverse types of crops identified in the area for four different growth stages and their related periods. Due to lack of detailed space- and time-dependent irrigation data, here we use a constant field application efficiency value, set to the national average of 0.75 (Wriedt et al., 2009). For the evaluation of the actual evapotranspiration, potential evapotranspiration is first computed by (i) making use of the model provided by Hargreaves and Samani (1985) in non-irrigated regions and (ii) combining the Penman–Monteith model with the correction crop coefficient in cultivated areas (consistent with Allen et al., 1998). The latter method has been developed and widely applied for estimating evapotranspiration in irrigated soils. Actual evapotranspiration is then computed on the basis of the soil water content. If SWC is larger than the potential evapotranspiration, ET is equal to the potential evapotranspiration; otherwise, ET = SWC. Note that the Hargreaves–Samani and Penman–Monteith models are implemented without considering any corrections for wind effects, as the study area experiences weak surface winds, with an average wind speed of approximately $2\,\mathrm{m\,s^{-1}}$ (Bonafè et al., 2014). Overland outflow (or surface runoff) is evaluated upon making use the Soil Conservation Service (SCS) curve number (CN) method (Mishra and Singh, 2003). Note that the estimation of R_{off} requires the availability of maps of hydrological soil class and land cover type. Hydrological soil classes are assessed through the broadly used Rosetta software (Schaap et al., 2001) that makes use of physical soil attributes such as clay and sand soil content as well as soil bulk density. Given the presence of very cold temperatures in different periods of the year for a large portion of the study area, we include a runoff enhancement factor in the case of frozen ground, as proposed by Molnau and Bissell (1983). Finally, the overland inflow to a given cell is evaluated as the sum of R_{off} values computed for the uphill neighbor cells in the previous time step iteration. A workflow of the recharge modeling approach is offered in Fig. 3. Detailed information regarding all input values employed here can be found on an open-access code repository (https://doi.org/10.5281/zenodo.10013442, Manzoni, 2023).

3.2 Groundwater modeling approach

We build a large-scale groundwater model that covers an area of approximately $31\,500\,\mathrm{km}^2$ within the Po River district (see Fig. 1). The architecture of the subsurface system is assessed by curating information embedded in datasets from three distinct local authorities. In this sense, we obtain an original integration of data stemming from the hydrostratigraphic survey of Emilia-Romagna (Regione Emilia-Romagna, 1998), as well as from the regional water protection plans of the Lombardia (Regione Lombardia, 2016) and Piemonte (Regione Piemonte, 2022) regions. These studies provide information on the lateral extent and the bottom surface of the depositional group that includes the groundwater system. This

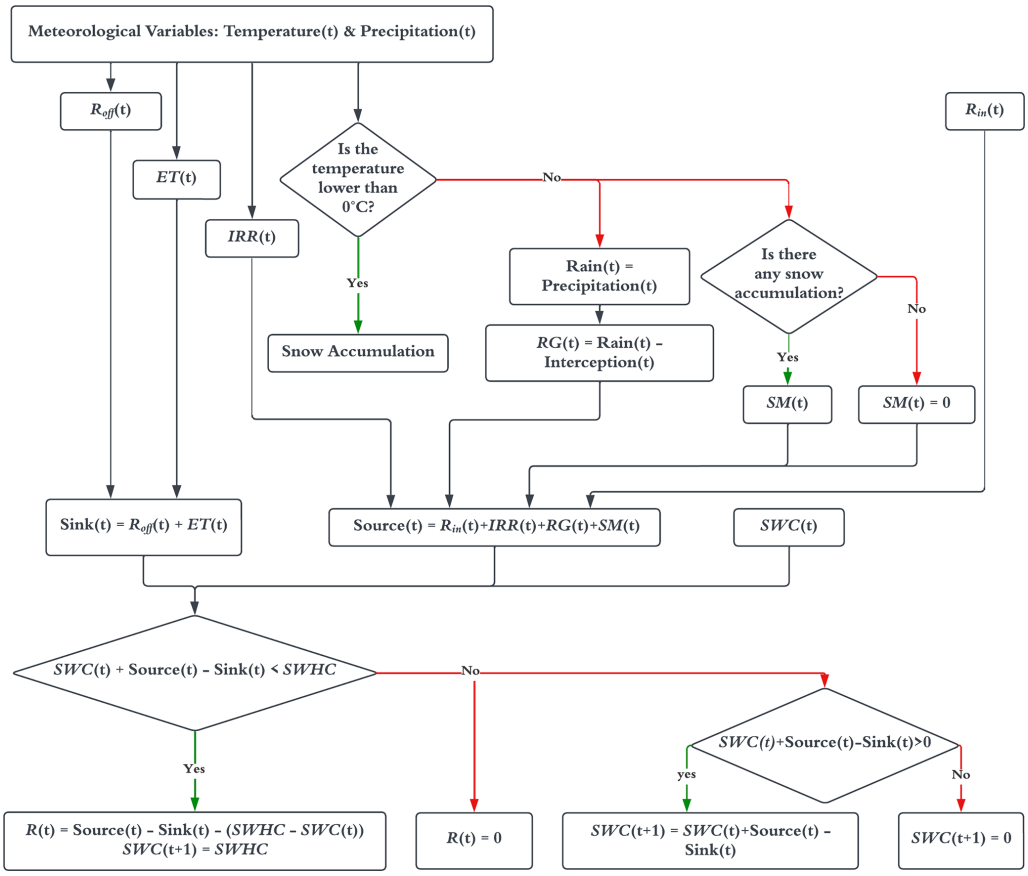

Figure 3. Conceptual workflow of the groundwater recharge model.

information has been obtained by local authorities upon integration of data from geological studies performed in the area. The evolution of the sedimentary basin, as controlled by geodynamic and climatological factors, is characterized by an overall regressive trend from Pliocene open marine facies to Quaternary marginal marine and alluvial deposits (Ricci Lucchi et al., 1982; Regione Emilia-Romagna and ENI-AGIP, 1998; Regione Lombardia and ENI-AGIP, 2002). The aquifer system is characterized by a dense network of deep faults that influence the overall depth of the aquifers (Carcano and Piccin, 2001), driving the variability in the groundwater system thickness from a few meters (close to the foothills) to more than 300 m (in the central and eastern portions of the plain). A continuous portion of virtually impermeable material can be found below the base surface. As already noted in Sect. 3.1, we employ a digital elevation model (ESA, 2019) to determine the topographic map of land surface. This information enables us to determine the boundary of the groundwater system. Notably, the highest uncertainties in the hydrostratigraphic reconstruction model are found beyond the lateral boundaries of the groundwater system, where only a limited number of investigations is available.

We discretize the three-dimensional subsurface domain through a hybrid mesh, as obtained within the Gmsh environment (Geuzaine and Remacle, 2009) through the OpenGeoSys Data Explorer GUI (Rink et al., 2013). The selected mesh enables us to capture the irregular shape of the boundaries of the investigated domain as well as its natural features while preserving the advantages of regular meshes for modeling layered geological systems. Domain discretization is performed according to a two-step approach. First, the ground surface is discretized using triangular elements with varying sizes (ensuring a maximum edge length of mesh elements of 5 km). Elements are adjusted to closely represent the ground surface as well as the irregular geometry of rivers and boundaries. The study employs a vertical discretization of the numerical grid that favors a balance between computational efficiency and the vertical distribution of geomaterials provided by the work of Manzoni et al. (2023). In this context, vertical discretization is finest near the surface, where thinner layers of geomaterials are documented. This is consistent with the availability of a high density of geological data at such depths, which has then facilitated identification of thin layers. Thus, the surface grid is then extruded along the vertical direction to the bottom surface underlying the whole groundwater system to create layers whose thick-

ness increases with depth according to the following criteria: (i) layers maintain a constant thickness of less than 10 m within the top 100 m below the surface level; (ii) at depths comprised between 100 and 200 m, the largest layer thickness is less than 20 m; and (iii) a constant thickness of less than 40 m is maintained for layers corresponding to depths larger than 200 m.

To determine the types of geomaterials associated with each cell of the resulting grid, we rely on the detailed three-dimensional probabilistic hydrostratigraphic model developed for the Po River district by Manzoni et al. (2023). The dataset includes six macro categories (or geomaterials, denoted as gravel, sand, silt, clay, fractured rock, and rock) according to which the data associated with lithostratigraphic information across the area can be grouped. Manzoni et al. (2023) rely on a fine structured grid (resolution of 1000×1000 m along the horizontal plane and 1 m along the vertical direction) and evaluate the probability that each cell is associated with one of these six geomaterials. On these bases, we can evaluate the fraction of the cth geomaterial that can be assigned to the ith cell of our simulation grid, $f_{c,i}$, as

$$f_{c,i} = \frac{1}{N_i} \sum_j^{N_i} P_{c,j} \,. \tag{2}$$

Here, N_i denotes the number of cells associated with the hydrostratigraphic model of Manzoni et al. (2023) that are included in the ith cell of our simulation grid and $P_{c,j}$ is the probability that the cth category (or geomaterial) be assigned to cell j of the abovementioned hydrostratigraphic model. Figure 4a depicts the percentage of simulation grid cells associated with given (color-coded) ranges of values for $f_{c,i}$ for each geomaterial category. One can note that clay and sand are the most abundant geomaterial categories identified across our domain. Otherwise, gravel is the most frequent among the remaining categories, being associated with about 15 % of the simulation grid cells. Categories associated with silt or rock and fractured rock are found in very limited proportion across the entire simulated domain.

Figure 4b illustrates the spatial distribution of the most probable geomaterial category within the Po River basin, as obtained by Manzoni et al. (2023). The reconstruction extends to a depth of 400 m below ground surface, covering the entire Po watershed and encompassing the full extent of the simulation grid.

We then assess the permeability of the ith cell of the grid as

$$\overline{k}_i = \sum_c^{N_c} f_{c,i}\, k_c \;\; \text{with} \;\; N_c = 6 \,, \tag{3}$$

where k_c is the permeability of the cth category; k_c values are estimated through model calibration, while $f_{c,i}$ is provided as prior information (see Manzoni et al., 2023). Details regarding model calibration are illustrated in Sect. 3.3.

As boundary conditions, we set a constant hydraulic head, $h = 0$ m, along the coastline and a Cauchy boundary condition along the Adige River. Flow boundary conditions are imposed along the remaining lateral boundaries (see Fig. 1). Here, boundary fluxes are assigned using a mass balance analysis performed across the 14 main sub-basins surrounding the investigated subsurface domain (denoted as sub-basins, $s = 1, 2, \ldots, 14$, in Fig. 1). The delineation of these sub-basins is provided by the Po River District Basin Authority (AdB-Po, 2021). Inflow takes place through the vertical surface that extends from the ground surface to the aquifer base along the lateral extent of the aquifer system. Such a lateral surface is typically characterized by a limited depth (only a few meters). Thus, lateral inflow is distributed uniformly across all layers of the lateral surface associated with each sub-basin. Making use of the results of Sect. 3.1, we evaluate within each of these sub-basins the average (in time) amount of water that infiltrates within a day as

$$Q_\mathrm{s} = r_q R'_\mathrm{s} S_\mathrm{s} \,, \tag{4}$$

where R'_s [$\mathrm{L\,T^{-1}}$] is the (space–time-averaged) recharge rate evaluated for the sth sub-basin (with a ground surface area of the extent of S_s) during the temporal window spanning the years 2013–2019. To account for possible exfiltration of infiltrated water or infiltration of water due to surface–groundwater interaction (e.g., river water infiltration), we also introduce a correction coefficient, r_q. The latter is set at a constant value for all sub-basins to avoid model overparameterization and is estimated through model calibration, as detailed in Sect. 3.3. Finally, we determine a uniform flow rate boundary condition for the sth sub-basin as $q_\mathrm{s} = Q_\mathrm{s}/A_\mathrm{s}$, A_s corresponding to the lateral surface associated with a given sub-basin. We assign water flow rate boundary conditions at the ground surface of the domain upon considering the mean groundwater recharge (see Sect. 3.3) and domestic water use. To estimate the volumetric flow rate for domestic use, we rely on the public water supply data provided by the Italian National Institute of Statistics (ISTAT, 2020). This dataset contains values of flow rates (in $\mathrm{m^3\,yr^{-1}}$) employed for domestic purposes for each municipal administrative area as well as the share of domestic water associated with groundwater resources. Such data are available for the years 2012, 2015, 2018, and 2020. We then evaluate the average flow rate for each municipality on this basis. For a given municipality, domestic water fluxes associated with the use of groundwater resources is assessed upon evaluating the ratio of the total volumetric flow rate associated with groundwater extractions for drinking water to the surface area covered by the municipality itself (OpenStreetMap, 2021). Volumetric flow rates employed in the model are then obtained by multiplying the portion of the municipality area within the modeled domain by the domestic water flux. Due to the lack of comprehensive information regarding the location of extraction wells, we consider such a water flow rate a distributed sink term located within the deepest layer of the simulation domain beneath each associated municipality. This assumption is grounded on the notion that drinking water wells are typically engineered to extract water from locations that are

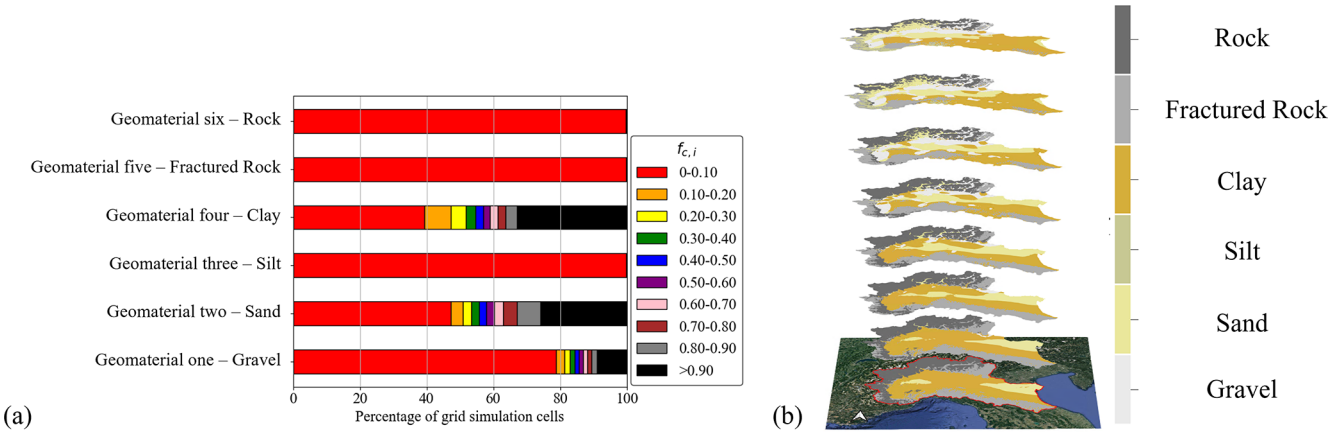

Figure 4. **(a)** Percentage of grid cells characterized by given ranges of values of $f_{c,i}$ (Eq. 2). **(b)** Spatial distribution of modal categories obtained by Manzoni et al. (2023). Planar maps are selected at 5, 10, 25, 50, 100, 150, 200, and 350 m below ground surface. Background map: © Google Maps 2023.

protected from potential contaminants that may infiltrate and pollute shallower regions of subsurface waterbodies. Finally, we set Robin boundary conditions along the cells associated with the main 18 rivers located within the domain (see Fig. 1 for their location), i.e.,

$$Q_{r,i} = -C_{r,i}\left(h_i - h_{\mathrm{rs},i}\right), \tag{5}$$

where $Q_{r,i}$ represents the water flow rate from the segment of the rth river of length $L_{r,i}$ within the ith grid cell to the groundwater systems; $C_{r,i}$ represents the riverbed conductance of segment $L_{r,i}$; and h_i and $h_{\mathrm{rs},i}$ are the groundwater hydraulic head at cell i and the elevation of the river stage of segment $L_{r,i}$, respectively. Each river is assigned a uniform specific conductance, $\alpha_r = C_{r,i}/L_{r,i}$, with the exception of the Po River. The latter is subdivided into three segments (see Fig. 1), each with a different specific conductance due to the varying geological characteristics, i.e., (i) the eastern portion of the river flows over a geologic region mainly characterized by deltaic, floodplain, coastal, and wind deposits; (ii) the middle portion of the river flows over a geologic region mainly characterized by terraced alluvium and aeolian deposits; and (iii) the western portions of the river meander through hilly regions, which exhibit diverse geological features (Compagnoni et al., 2004). This subdivision leads to 20 distinct values of α_r, estimated as detailed in Sect. 3.3.

3.3 Calibration data and inverse modeling strategy

In this section, we first report on the procedures applied to obtain calibration data from raw datasets (Sect. 3.3.1), and then we describe the main traits of the model inversion strategies (Sect. 3.3.2).

3.3.1 Data curation

Model parameters are estimated using time-averaged measurements of groundwater levels available across the domain and collected between January 2013 and December 2019. These data are available for the three main Italian regions within which the groundwater system resides (i.e., Piemonte, Lombardia, and Emilia-Romagna). Available data are not homogeneous in terms of quantities monitored, temporal windows associated with data collection, and data format. Data curation is therefore a critical element to enable effective use of the available information. The resulting dataset is presented and employed for the first time here. It serves as a basis upon which future studies aimed at further enhancing our knowledge of the hydrological functioning of this large-scale groundwater system and designing appropriate water management strategies therein can be developed.

Hydraulic head data have been collected with a sampling frequency of 8 h for the Piemonte region (Agenzia Regionale per la Protezione Ambientale Piemonte, 2020). In the Emilia-Romagna and Lombardia regions, the sampling frequency varies among wells, with an average approximately corresponding to 2 and 10 samples per year, respectively (Regione Emilia-Romagna, 2020; Regione Lombardia, 2021). We apply a filtering process to the raw data before combining the different datasets. To avoid seasonal biases, we exclude from the dataset wells that do not have at least one observation in two different seasons for each year within the given time range. Furthermore, we exclude observation wells affected by local operational activities. For the $N_{h_b} = 286$ remaining wells, whose locations are indicated in Fig. 1, we evaluate the average hydraulic head, $\overline{h_l}$ (with $l = 1, \ldots, N_{h_b}$), associated with the investigated period.

3.3.2 Model calibration

Model parameters are estimated through a multi-objective optimization approach. The latter is tied to the joint minimization of two objective functions formulated as

$$f_{N_{h_b}} = \sqrt{\frac{\sum_{l=1}^{N_{h_b}} \left(\overline{h_l} - h_l\right)^2}{N_{h_b}}} \tag{6}$$

and

$$f_{N_{h_r}} = \sqrt{\frac{\sum_{l=1}^{N_{h_r}} \left(\overline{h_l} - h_l\right)^2}{N_{h_r}}}, \tag{7}$$

where $\overline{h_l}$ and h_l denote observed and estimated hydraulic head at well l, respectively. Estimation of permeability of each geomaterial (i.e., k_c in Eq. 3) and of the correction coefficient (i.e., r_q in Eq. 4) entails minimizing Eq. (6) (considering all available hydraulic head data, N_{h_b}). To estimate the specific conductance of the riverbeds, α_r (with $r = 1, \ldots, 20$), we minimize Eq. (7) with $N_{h_r} < N_{h_b}$, where N_{h_r} is the number of wells located within a maximum distance of 5 km from a river (see orange dots in Fig. 1). Including this constraint on the distance between a river and observation wells enables us to refine the estimation of α_r by considering only hydraulic head observations that are significantly impacted by the interconnection between the groundwater system and the rivers. Note that minimization of Eqs. (6) and (7) is tantamount to relying on a maximum likelihood (ML) estimation approach, assuming that measurement errors in hydraulic head are not correlated and can be described through a Gaussian distribution (Carrera and Neuman, 1986). The two objective functions to minimize are closely interconnected. We implement an enhanced variant of the differential evolution (DE) optimization method (Storn and Price, 1997) to effectively minimize both objective functions simultaneously. Here, we rest on a modified version of the Cooperative Coevolutionary Differential Evolution (CCDE) optimization algorithm proposed by Trunfio (2015). The implemented algorithm does not require defining a single weighted multi-objective function, as otherwise required by standard DE and standard CCDE. Thus, our approach eliminates the non-trivial task of determining the appropriate (relative) weights between each of the terms that constitute the multi-objective function (e.g., Dell'Oca et al., 2023). Resorting to a modified CCDE algorithm enables us to balance between simplicity and the efficiency documented for coevolutionary algorithms (CAs) when dealing with multi-objective fitness functions (Khan et al., 2022).

As nature-inspired optimization techniques, CAs draw upon principles of biological coevolution, where optimization problems are linked to coevolving species (Dagdia and Mirchev, 2020). CAs share similarities with evolutionary algorithms, as their sampling mechanisms and dynamics are inspired by Darwin's theory of evolution. Just as species evolve based on their fitness to survive and reproduce within an environment, solutions within a search space evolve to achieve the minimum of an objective function (Simoncini and Zhang, 2019). Additionally, the coevolution principle considers that a change in one species can trigger changes in related species, thus leading to adaptive changes in each species (Khan et al., 2022). In this context, Eqs. (6) and (7) represent optimization functions for two coevolving species. These are then optimized through the modified CCDE. Our algorithm differs from CCDE (Trunfio, 2015) primarily in the way we define the dimensions of the two species. Instead of employing random or dynamic grouping strategies (Yang et al., 2008; Trunfio, 2015), we opt for a supervised grouping strategy linking one of the model parameters (i.e., riverbed conductance, α_r) to one species and the remaining parameters to the other species.

We choose a modified version of Coevolutionary Differential Evolution (CCDE) over the widely used NSGA-II (or its variant, CC-NSGA-II) for our algorithm. Both these algorithms use a divide-and-conquer strategy and are effective for high-dimensional optimization. However, while NSGA II relies on a genetic algorithm, our algorithm utilizes differential evolution (DE). According to Tusar and Filipic (2007), DE-based algorithms outperform GA-based algorithms in multi-objective optimization due to a more efficient exploration of the parameter space. This element is particularly critical when optimal solutions lie on parameter bounds or amidst many local optima.

Additionally, our implemented algorithm does not explicitly optimize a *front*, which is otherwise a central concept in NSGA-II. Instead, it focuses on optimizing individual objective function values without introducing a dominance concept considering both objectives. This approach leads to a single set of optimized parameters, thus simplifying the optimization process through a balance of the contribution of both objective functions.

The implemented algorithm is designed to address global optimization problems through alternate evolution of candidate solutions between the two different species. The algorithm uses mutation, crossover, and selection strategies to enhance the quality of solutions, as detailed in the following. First, we introduce the populations of candidate solutions. For each of the two species (where sp takes the value of 1 or 2, for species associated with Eqs. 6 and 7, respectively), we consider a set of N_S candidate solutions (or members), denoted as $\boldsymbol{S}_{\mathrm{sp}} = \left[\boldsymbol{s}_{\mathrm{sp},1}, \ldots, \boldsymbol{s}_{\mathrm{sp},m}, \ldots, \boldsymbol{s}_{\mathrm{sp},N_s}\right]$. Following Storn and Price (1997), we set $N_S = 15 \times N_p$, N_p being the number of parameters (i.e., $N_p = 7$ or 20 for Eq. 6 or Eq. 7, respectively). Initial candidate solutions are defined by randomly selecting parameter values from a parameter space whose extent is designed to encompass a broad range of possible solutions.

Members of the populations are combined and mutated to calculate the next generations of candidate solutions as fol-

lows. We start by computing a mutated vector for each mth candidate solution of a species associated with the kth iteration of the optimization algorithm (or generation) as

$$\hat{\boldsymbol{s}}^k_{\mathrm{sp},m} = \boldsymbol{s}^k_{\mathrm{sp},m} + F\left(\boldsymbol{s}^k_{\mathrm{sp},a} - \boldsymbol{s}^k_{\mathrm{sp},b}\right). \tag{8}$$

Here, F represents an algorithm parameter (termed differential weight) that is set to be equal to 0.5 and $\boldsymbol{s}^k_{\mathrm{sp},a}$ and $\boldsymbol{s}^k_{\mathrm{sp},b}$ (with $a \neq b \neq m$) correspond to two (randomly selected) members of the population. We then combine parameters of $\hat{\boldsymbol{s}}^k_{\mathrm{sp},m}$ and $\boldsymbol{s}^k_{\mathrm{sp},m}$ to determine the trial vector $\tilde{\boldsymbol{s}}^k_{\mathrm{sp},m}$: if a parameter of $\tilde{\boldsymbol{s}}^k_{\mathrm{sp},m}$ is selected for mutation, its value is taken from $\hat{\boldsymbol{s}}^k_{\mathrm{sp},m}$; otherwise, it is taken from $\boldsymbol{s}^k_{\mathrm{sp},m}$. We randomly choose the parameters of $\boldsymbol{s}^k_{\mathrm{sp},m}$ that will undergo mutation among the parameters associated with the sp species, with a probability of parameter mutation set to 0.5. We finally select the mth candidate solution of the $(k+1)$th generation, $\boldsymbol{s}^{k+1}_{\mathrm{sp},m}$, by comparing the trial member, $\tilde{\boldsymbol{s}}^k_{\mathrm{sp},m}$, and the mth population member from the kth generation, $\boldsymbol{s}^k_{\mathrm{sp},m}$, based on the following condition:

$$\boldsymbol{s}^{k+1}_{\mathrm{sp},m} = \begin{cases} \tilde{\boldsymbol{s}}^k_{\mathrm{sp},m} & \text{if } f_N\left(\tilde{\boldsymbol{s}}^k_{\mathrm{sp},m}\right) < f_N\left(\boldsymbol{s}^k_{\mathrm{sp},m}\right), \\ \boldsymbol{s}^k_{\mathrm{sp},\,m} & \text{if } f_N\left(\tilde{\boldsymbol{s}}^k_{\mathrm{sp},m}\right) \geq f_N\left(\boldsymbol{s}^k_{\mathrm{sp},m}\right), \end{cases}$$

$$\text{with } f_N = f_{N_{h_l}} \text{ or } f_{N_{h_r}}. \tag{9}$$

The algorithm steps can be summarized as follows at a given iteration k:

1. A new generation $(k+1)$ of the first species is calculated using Eqs. (8)–(9), with $f_N = f_{N_{h_l}}$, while keeping the parameters of the second species fixed.

2. The parameter set with the best performance, $\boldsymbol{s}^{k+1}_{1,\mathrm{best}}$, among the members of $\boldsymbol{s}^{k+1}_{1,m}$ is transferred to the second species.

3. The parameters of the first species are maintained as fixed while calculating $\boldsymbol{s}^{k+1}_{2,m}$ (the next generation of the second species), thus repeating step 1 for the second species with sp = 2 and Eq. (7).

4. The parameter set of the member in the second species with the best objective function value, $\boldsymbol{s}^{k+1}_{2,\mathrm{best}}$ is passed back to the first species.

5. Steps 1 to 4 are repeated until a stopping criterion is met.

The patience stopping criterion is employed here for both objective functions; i.e., the algorithm stops if no improvement in performance over 80 consecutive iterations (or epochs) is detected. Figure 5 illustrates the pseudocode of the algorithm.

```
Begin
  Initialize S_1 = [s_{1,1}, ..., s_{1,m}, ... , s_{1,N_s1}] and S_2 = [s_{2,1}, ..., s_{2,m}, ... , s_{2,N_s2}].
  Evaluate the members of S_1 using Eq. (6).
  Evaluate the members of S_2 using Eq. (7).
  While stopping criteria are not met for both the species:
    For each m-th member of S_1
      Create s̃^k_{1,m} by applying mutation and crossover.
      Evaluate s̃^k_{1,m} using Eq. (6).
      Select s^{k+1}_{1,m} according to Eq. (9).
      Select s^{k+1}_{1,best}
    EndFor
    Fix the parameters associated with Eq. (6) equal to s^{k+1}_{1,best}.
    For each m-th member of S_2
      Create s̃^k_{2,m} by applying mutation and crossover.
      Evaluate s̃^k_{2,m} using Eq. (7).
      Select s^{k+1}_{2,m} according to Eq. (9).
      Select s^{k+1}_{2,best}
    EndFor
    Fix the parameters associated with Eq. (7) equal to s^{k+1}_{2,best}.
    k++
  EndWhile
  Return s^{k+1}_{2,best} and s^{k+1}_{1,best}.
End
```

Figure 5. Pseudocode of the employed algorithm.

Finally, to quantify the residual (i.e., after calibration) uncertainty associated with each estimated model parameter, we compute the parameter estimation covariance matrix, $\boldsymbol{\Sigma}_N$, as

$$\frac{\boldsymbol{\Sigma}_N}{\sigma^2_{h,N}} = \left[\mathbf{J}^T\,\mathbf{J}\right]^{-1}, \text{ with } N = N_{h_b}, N_{h_r}, \tag{10}$$

where $\mathbf{J}$ is the Jacobian matrix (T denoting transpose) of size $[N \times N_p, N_p]$ and $\sigma^2_{h,N}$ is measurement error variance. The latter is generally unknown and can be computed a posteriori, as detailed in Carrera and Neuman (1986). Matrix $\mathbf{J}$ contains the derivatives of h with respect to model parameters. These are evaluated at the end of the optimization procedure using a centered difference scheme.

3.4 Global sensitivity analysis

A global sensitivity analysis is performed in the surrounding of the parameter values obtained through model calibration. A GSA provides valuable insights into the impact of parameter uncertainty in the simulated variable (i.e., hydraulic head values in our case). Furthermore, an informed GSA offers guidance about where new (hydraulic head) measurements can enhance the quality of parameter estimates. As a GSA metric, we rely on the Morris indices. These are defined

through the introduction of elementary effects, $\mathrm{EE}_{\theta_{p,n}}$.

$$\mathrm{EE}_{\theta_{p,n}} = \frac{h\left(\theta_1,\ldots,\theta_p+\Delta\theta_p,\ldots,\theta_{N_p}\right)-h\left(\theta_1,\ldots,\theta_p,\ldots,\theta_{N_p}\right)}{\Delta\theta_p} \quad (11)$$

Here, $\mathrm{EE}_{\theta_{p,n}}$ is the incremental ratio for the uncertain parameter θ_p computed along trajectory n within the parameter space and $\Delta\theta_p$ is an increment evaluated as proposed by Campolongo et al. (2007). The Morris index, $\mu^*_{\theta_p}$, is then defined as

$$\mu^*_{\theta_p} = \frac{1}{M}\sum\nolimits_n^M \left|\mathrm{EE}_{\theta_{p,n}}\right| . \quad (12)$$

Here, M represents the number of trajectories (i.e., the number of diverse parameter combinations) selected employing a radial-sampling strategy (Campolongo et al., 2007). Stable results have been obtained with $M = 500$, requiring $(M+1)\,N_P$ forward model simulations. We recall that the absolute value in Eq. (12) prevents cancellation between positive and negative values of $\mathrm{EE}_{\theta_{p,n}}$. Variations in the value of parameters associated with low values of $\mu^*_{\theta_p}$ induce negligible changes in h. Note that we evaluate $\mu^*_{\theta_p}$ at all spatial locations within the simulated domain. This enables us to create a three-dimensional spatial distribution of Morris indices, providing insights into the impact of each parameter on hydraulic head values across the entire domain.

4 Results and discussion

This section is devoted to the discussion of the results related to the groundwater recharge spatial distribution (Sect. 4.1), groundwater flow model calibration and simulations (Sect. 4.2), and global sensitivity analysis (Sect. 4.3).

We begin by examining the spatial distribution of groundwater recharge and its impacts on the groundwater flow model. Our discussion encompasses model parameterization results and the large-scale three-dimensional flow patterns obtained through the calibrated model. The insights gained from model calibration assist the definition of an informed parameter space for the subsequent GSA.

4.1 Groundwater recharge

Figure 6 depicts (time-averaged, during the years 2013–2019) spatial distribution of estimated annual groundwater recharge. The highest rates of recharge are detected in the northern part of the domain, which is characterized by high precipitation levels and permeable geomaterials (Poggio et al., 2021). The eastern area of the domain exhibits shallow groundwater conditions and low permeability geomaterials, resulting in reduced infiltration rates. These findings are consistent with the spatial distribution of groundwater recharge presented by Rossi et al. (2022). These authors estimate groundwater recharge in Italy using a water balance approach and open-access data while relying on a spatial resolution that is otherwise coarser that the one we consider (i.e., grid-cell resolution of 10×10 km). Their study places annual groundwater recharge for the Po River watershed at values ranging between 27 and $37 \times 10^9\ \mathrm{m^3\,yr^{-1}}$. Our calculated average annual groundwater recharge for the entire watershed for the period 2013–2019 corresponds approximately to 38 billion $\mathrm{m^3\,yr^{-1}}$ and is thus in line with the above-mentioned range.

Most of the groundwater recharge takes place in the mountain areas of the Po River district, with only approximately 0.4 billion $\mathrm{m^3\,yr^{-1}}$ being received from the top surface of the aquifer. This result suggests that the main water inflow to groundwater is related to the lateral surface located close to the foothills.

4.2 Groundwater model

To ensure effective convergence of the CCDE algorithm, we rely on the set of metrics depicted in Fig. 7a–d. Note that the optimization algorithm leads to a converge of both objective functions (f_{N_b} and f_{N_r}) in less than 50 iterations. The ensuing calibrated model is seen to display a remarkable degree of consistency with the system behavior observed across the domain (see Fig. 7c, d). The mean absolute error (in terms of hydraulic head) in the central and eastern areas of the Po Plain is consistently low, averaging about 4.5 m for these regions. The highest errors are observed near the foothill areas and in the planar areas of the Piemonte region. Estimated model parameter values are listed in Table 1.

Results associated with the entries of the parameter estimation covariance matrices ($\mathbf{\Sigma}_{N_b}/\sigma^2_{h,N_b}$ and $\mathbf{\Sigma}_{N_r}/\sigma^2_{h,N_r}$) are depicted in Fig. 8a and b, respectively. As shown by the diagonal terms in Fig. 8a, the estimation variance of permeability (k) is higher for geomaterial categories five (fractured rock) and six (rock) as compared to the other ones. This result is related to the observation that these geomaterials are present in small amounts within the domain (see Fig. 4). Furthermore, there is a certain degree of negative correlation between permeabilities of geomaterial five and r_q. This finding is attributed to the fact that the simulation grid cells with the highest proportion of geomaterial five can be found in the mountainous areas and near the foothills (see Fig. 4b), which are close to the boundary where an inflow boundary condition is applied. Therefore, in these locations, an increase (or decrease) in the inflow across the boundaries can be obtained by increasing (or decreasing) both k_5 and r_q.

When considering riverbed conductance, it is observed that rivers with lower flows, such as the Chiese, Lamone, Savio, and Sesia rivers (associated with parameters α_5, α_{12}, α_{13}, and α_{17}; see Fig. 1 for their planar location), exhibit the largest parameter estimation variance. In the central part of the Po River, the estimation variance of α_{10} is generally low. This suggests that the available data can effectively inform and provide valuable insights into the dynamics of river–

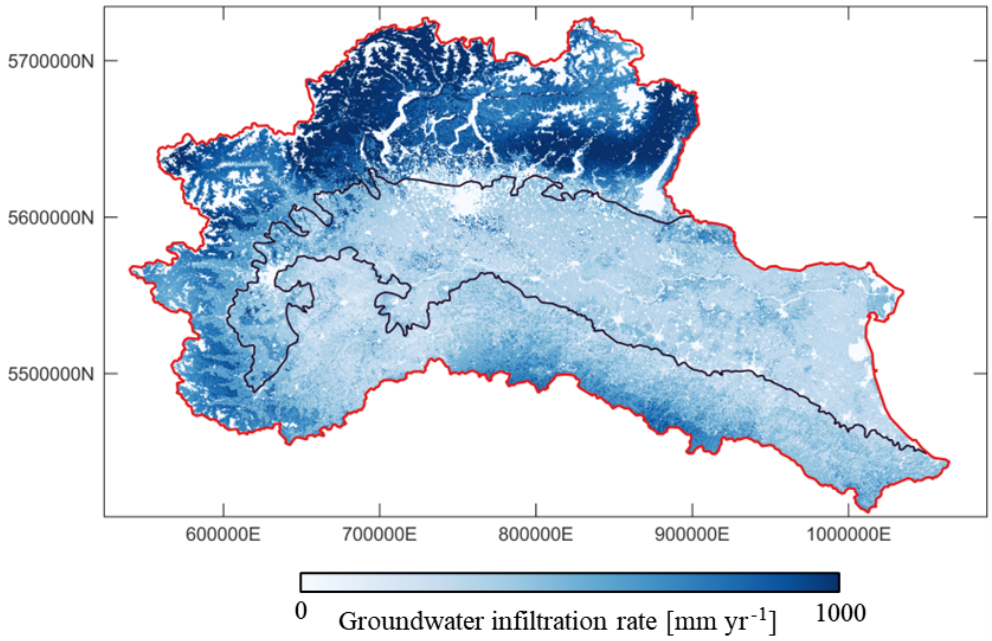

Figure 6. Estimated mean annual groundwater recharge across the Po River district. The coordinate reference system (CRS) is ESRI:54012.

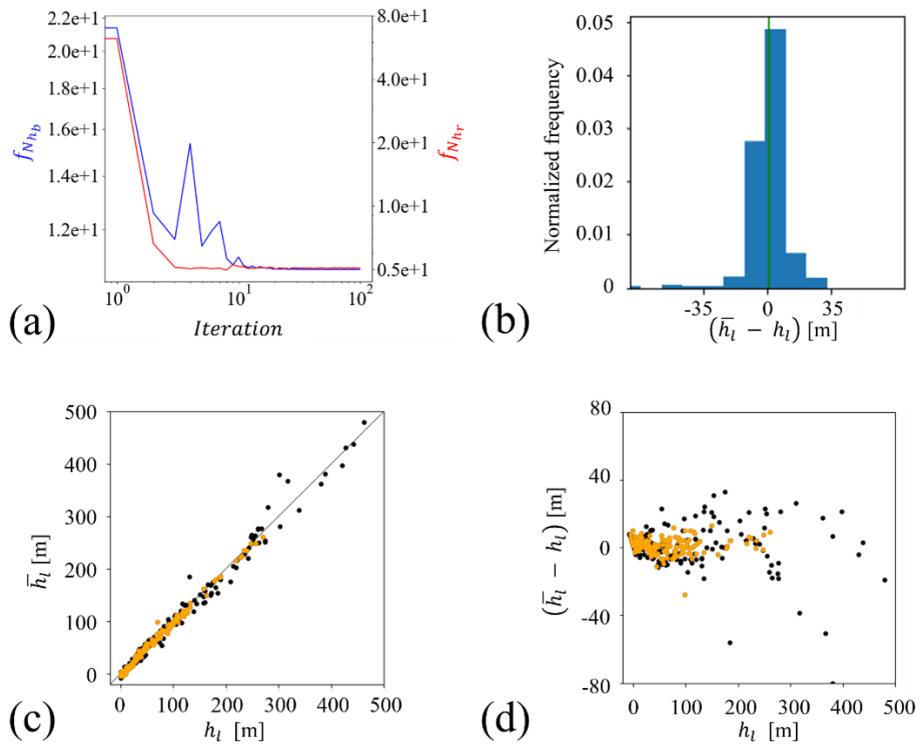

Figure 7. **(a)** Convergence analysis of f_{N_b} and f_{N_r} (Eqs. 6 and 7, respectively), **(b)** normalized frequency distribution of differences between observed ($\overline{h_l}$) and simulated (h_l) hydraulic heads, **(c)** observed versus simulated hydraulic heads (values associated with the N_{h_r} wells located close to the rivers are depicted in orange), and **(d)** post-calibration residuals ($\overline{h_l} - h_l$) versus observed heads.

Table 1. Uncertain model parameters, associated estimated values resulting from model calibration, and intervals of variability employed in the GSA.

Parameter	Description	Parameter estimate	Parameter range of variability
$k_1 \times 10^{-9}$ [m^2]	Permeability of geomaterial one	1.02	0.64–1.61
$k_2 \times 10^{-9}$ [m^2]	Permeability of geomaterial two	3.83	2.24–6.08
$k_3 \times 10^{-13}$ [m^2]	Permeability of geomaterial three	2.24	1.41–2.55
$k_4 \times 10^{-10}$ [m^2]	Permeability of geomaterial four	1.57	0.99–2.49
$k_5 \times 10^{-15}$ [m^2]	Permeability of geomaterial five	2.12	1.34–3.37
$k_6 \times 10^{-18}$ [m^2]	Permeability of geomaterial six	5.04	3.18–8.00
r_q [–]	Lateral inflow correction coefficient	0.99	0.79–1.19
$\alpha_1 \times 10^{-5}$ [m^2 s^{-1}]	Specific conductance of Adige	8.18×10^{-2}	8.18×10^{-4}–8.18
$\alpha_2 \times 10^{-5}$ [m^2 s^{-1}]	Specific conductance of Secchia	7.12×10^{-2}	7.12×10^{-4}–7.12
$\alpha_3 \times 10^{-4}$ [m^2 s^{-1}]	Specific conductance of Dora Baltea	1.02×10^{-2}	1.02×10^{-4}–1.02
$\alpha_4 \times 10^{-7}$ [m^2 s^{-1}]	Specific conductance of Ticino	1.10×10^{-2}	1.10×10^{-4}–1.10
$\alpha_5 \times 10^{-3}$ [m^2 s^{-1}]	Specific conductance of Chiese	3.34×10^{-2}	3.34×10^{-4}–3.34
$\alpha_6 \times 10^{-7}$ [m^2 s^{-1}]	Specific conductance of Oglio	2.44×10^{-2}	2.44×10^{-4}–2.44
$\alpha_7 \times 10^{-5}$ [m^2 s^{-1}]	Specific conductance of Tanaro	3.04×10^{-2}	3.04×10^{-4}–3.04
$\alpha_8 \times 10^{-2}$ [m^2 s^{-1}]	Specific conductance of Po – western section	2.95×10^{-2}	2.95×10^{-4}–2.95
$\alpha_9 \times 10^{-2}$ [m^2 s^{-1}]	Specific conductance of Po – eastern section	1.34×10^{-2}	1.34×10^{-4}–1.34
$\alpha_{10} \times 10^{-4}$ [m^2 s^{-1}]	Specific conductance of Po – central section	1.16×10^{-2}	1.16×10^{-4}–1.16
$\alpha_{11} \times 10^{-5}$ [m^2 s^{-1}]	Specific conductance of Reno	2.90×10^{-2}	2.90×10^{-4}–2.90
$\alpha_{12} \times 10^{-5}$ [m^2 s^{-1}]	Specific conductance of Lamone	5.53×10^{-2}	5.53×10^{-4}–5.53
$\alpha_{13} \times 10^{-2}$ [m^2 s^{-1}]	Specific conductance of Savio	7.50×10^{-2}	7.50×10^{-4}–7.5
$\alpha_{14} \times 10^{-5}$ [m^2 s^{-1}]	Specific conductance of Adda	3.20×10^{-2}	3.20×10^{-4}–3.20
$\alpha_{15} \times 10^{-5}$ [m^2 s^{-1}]	Specific conductance of Taro	1.83×10^{-2}	1.83×10^{-4}–1.83
$\alpha_{16} \times 10^{-8}$ [m^2 s^{-1}]	Specific conductance of Mincio	7.3×10^{-2}	7.30×10^{-4}–7.30
$\alpha_{17} \times 10^{-2}$ [m^2 s^{-1}]	Specific conductance of Sesia	2.16×10^{-2}	2.16×10^{-4}–2.16
$\alpha_{18} \times 10^{-4}$ [m^2 s^{-1}]	Specific conductance of Orco	1.79×10^{-2}	1.79×10^{-4}–1.79
$\alpha_{19} \times 10^{-4}$ [m^2 s^{-1}]	Specific conductance of Lambro	4.39×10^{-2}	4.39×10^{-4}–4.39
$\alpha_{20} \times 10^{-6}$ [m^2 s^{-1}]	Specific conductance of Naviglio Grande	1.03×10^{-2}	1.03×10^{-4}–1.03

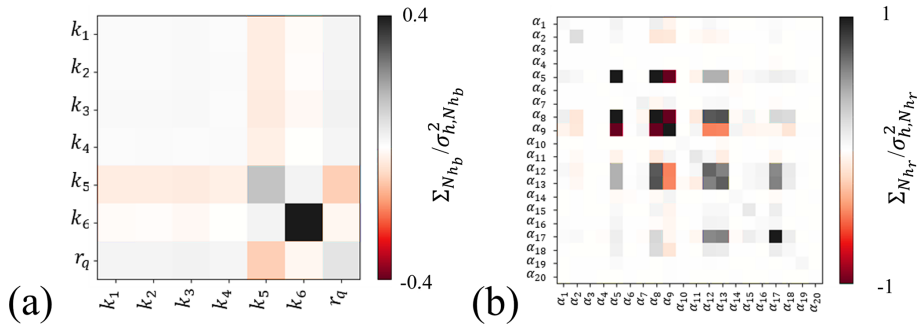

Figure 8. Covariance matrix of parameter estimates related to **(a)** Eq. (6) and **(b)** Eq. (7).

groundwater interactions in this area. Conversely, estimates of parameters α_8 and α_9, characterizing the western and eastern portion of Po River, are associated with a high estimation variance. Additionally, a negative correlation can be observed between α_8 and α_9.

Figure 9 offers an overview of the three-dimensional distribution of permeability values across the subsurface domain. Figure 9a depicts the frequency distribution of the estimated permeabilities. These results reveal three dominant modes (or peaks) in the distribution. These are characterized by a frequency that is 1 order of magnitude higher with respect to the rest of permeability values. This element suggests that the subsurface domain can be conceptualized (at this large scale) as a block-heterogeneous system comprising three main macro-areas, each of these being characterized by a mildly heterogeneous spatial distribution of permeability values. In this sense, the extent of each of these areas is assessed on the basis of the distribution of geo-

materials, which in turn drives the spatial distribution of permeability. The spatial arrangement of these macro-areas is consistent with the distribution of the three main sediment types indicated in the Italian geological map (Compagnoni et al., 2004) within the Po Plain (see Fig. 9c). Figure 9a provides an appraisal of the spatial distribution of the three macro-areas by means of envelopes obtained through projection of their otherwise three-dimensional shape on a two-dimensional (2D) plane. This visualization is complemented by Fig. 9b, which depicts a qualitative representation of the vertical distribution of $\log(k)$ along selected cross sections (vertical exaggeration of 200). Access to a detailed grid of the three-dimensional distribution of permeability values is available through a code and data repository (https://doi.org/10.5281/zenodo.10013442, Manzoni, 2023).

The first macro-area, associated with the lowest permeability values within the modeled domain, generally corresponds to the southeastern portion of the alluvial plain (Adriatic sector). Here, finer and less permeable sediments constitute the main features associated with geological deposition processes. The second macro-area is primarily located near the northern and western boundary, adjacent to the Alpine foothill areas, and is characterized by intermediate permeability values. Additional smaller areas with conditions similar to the Alpine foothills can be identified in the foothill areas of the Apennines. Note that, according to Éupolis Lombardia (2016), the planar area adjacent to the foothills in the Lombardia region is very heterogeneous and features a series of highly permeable layers interspersed with less permeable layers. This is consistent with the intermediate range of permeability values obtained within our large-scale domain through model calibration. The third macro-area is characterized by high permeability values. It spans the entire depth of the system in the central-southern portion of the plain, while it does not reach the surface in the northeastern part of the domain. This area is influenced by the deposits formed by the presence of the Po River.

As shown in Fig. 10a, hydraulic heads exhibit a higher gradient on the western side of the domain. This behavior can be attributed to the shallow depth of the aquifer and to the steep gradient of the domain bottom in this area. Figure 10b illustrates the way velocity magnitude and pattern are influenced by the three-dimensional distribution of the geomaterials and the thickness of the domain. As exemplified in section A–A′, our results document that subsurface flow can be considered chiefly 2D (i.e., vertical flow is negligible) across regions where the groundwater system is very thin, and the bottom is fairly parallel to the ground surface. This is especially evident in the steepest areas within the domain. Other than that, velocity distributions across sections B–B′ and C–C′ exhibit marked three-dimensional characteristics in terms of flow. With reference to section C–C′, we note that lower permeability close to the domain bottom results in reduced groundwater fluxes, as compared to the other sections. Additionally, the bottom-right side of section B–B′ documents the impact of low-permeability lenses on the local three-dimensional patterns of fluxes (in terms of magnitude and direction). Finally, Fig. 10b documents spatial variability in permeability and groundwater flow across three selected vertical cross sections near the rivers, highlighting the effects of river–groundwater interactions.

4.3 Global sensitivity analysis

Ranges of parameter variability employed for the GSA are listed in Table 1. These are selected to allow for (approximately) a 100 % variability in permeabilities values, while values of parameter α_r $(r = 1, \ldots, 20)$ can vary by 4 orders of magnitude. This choice enables us to account for the extensive uncertainty associated with the quantification of the interconnections between subsurface and surface waterbodies, as these variables are typically not monitored in the field.

Figure 11 depicts values of $\mu^*_{\theta_p}$ associated with geomaterial permeability and correction coefficient r_q. These results suggest that permeability values of geomaterial categories three, five, and six have a negligible impact on the spatial distribution of hydraulic heads. We recall that categories three, five, and six are detected only in a limited amount within the modeled domain (see Fig. 4). As expected, the permeability of geomaterial one (gravel) significantly influences simulation results in the foothills of the western portion of the domain, while that of category four (clay) primarily affects simulation results in the southeastern portion of the domain. These results are in line with the spatial distribution associated with two lithologies. Category two (sand) displays a noticeable impact on the hydraulic head distribution across the entire domain, which aligns with the observation that it is a widely available geomaterial within the system, spanning from west to east. Finally, parameter r_q significantly impacts hydraulic heads within all foothill areas, where lateral flow enters the groundwater system. As expected, its importance gradually decreases when moving away from the boundary. The influence of permeability and r_q significantly diminishes near the main rivers, where the flow field is primarily affected by parameters related to riverbed conductance (Fig. 12). Most of the riverbed conductance values can only affect hydraulic head estimates close to the rivers. This enables us to quantify the extent of the river influence on groundwater flow and further supports our calibration strategy, i.e., the use of the designed multi-objective optimization approach.

Rivers with the highest flow rates, such as the Adige (α_1), Ticino (α_4), Oglio (α_6), Reno (α_{11}), and Adda (α_{14}), as well as the central section of the Po River (α_{10}), exhibit the highest values of $\mu^*_{\theta_p}$. Rivers like the Chiese River (α_5) and the western (α_8) and eastern part of the Po River exhibit limited impact on simulated hydraulic head fields, partially due to their proximity to specific boundaries. These boundaries primarily influence groundwater flow through lateral bound-

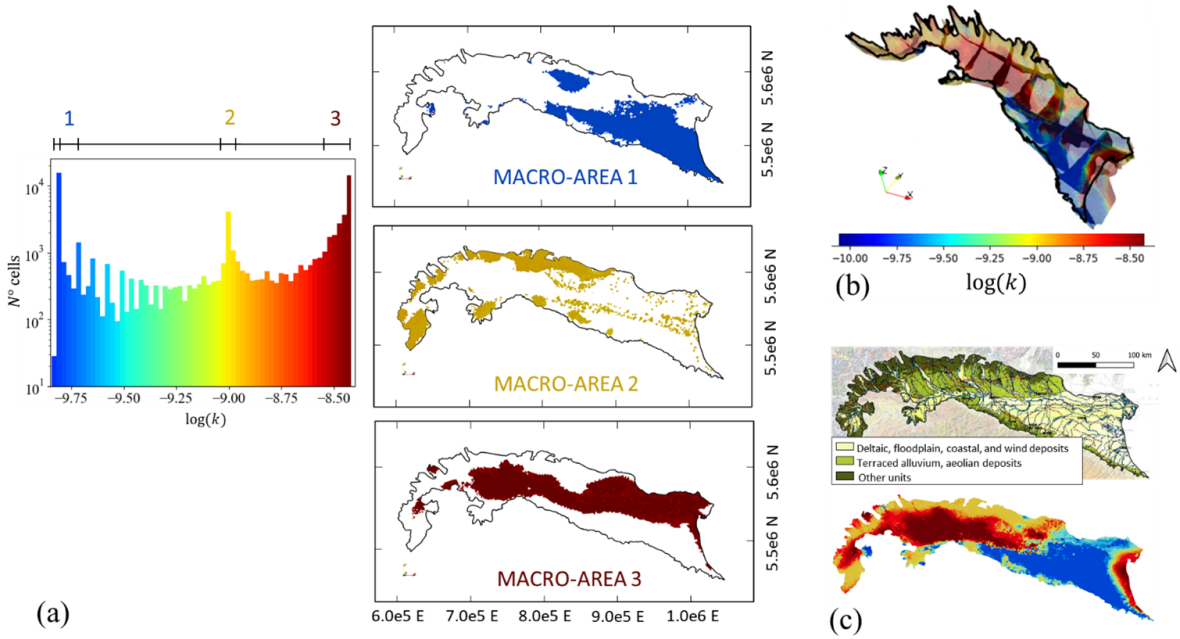

Figure 9. **(a)** Frequency distribution of the natural logarithm of permeability, $\log(k)$ (k expressed in m^2), estimates, and spatial distribution of the three macro-areas corresponding to envelopes obtained through projection of their otherwise three-dimensional shape on a 2D plane; **(b)** vertical distribution of $\log(k)$ along selected cross sections (vertical exaggeration of 100); and **(c)** visual comparison between the spatial distribution of permeability estimates across the model top layer and the distribution of the three main sediment types indicated in the Italian geological map (Compagnoni et al., 2004) within the Po Plain.

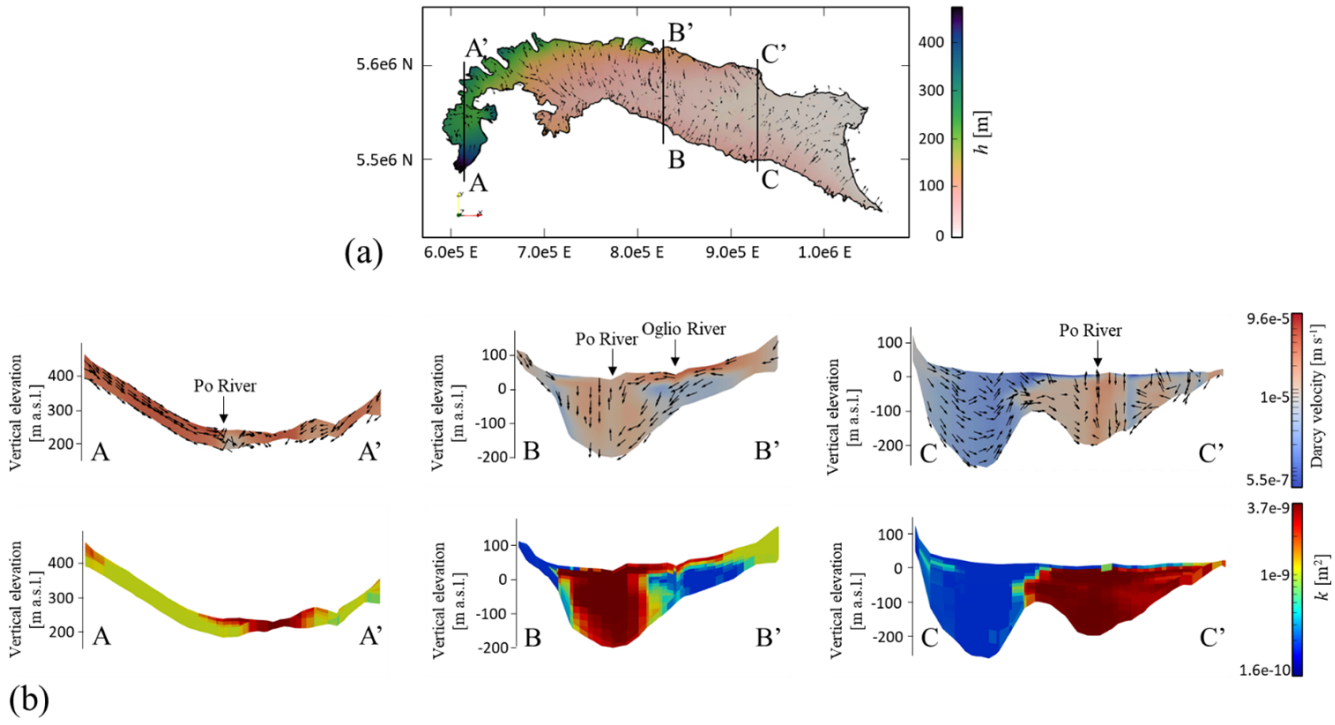

Figure 10. Main groundwater flow model outputs: **(a)** hydraulic head and overall direction of groundwater fluxes across the top layer of the model and **(b)** magnitude and overall direction of groundwater fluxes and permeability distribution along cross sections A–A′, B–B′, and C–C′ (vertical exaggeration of 200).

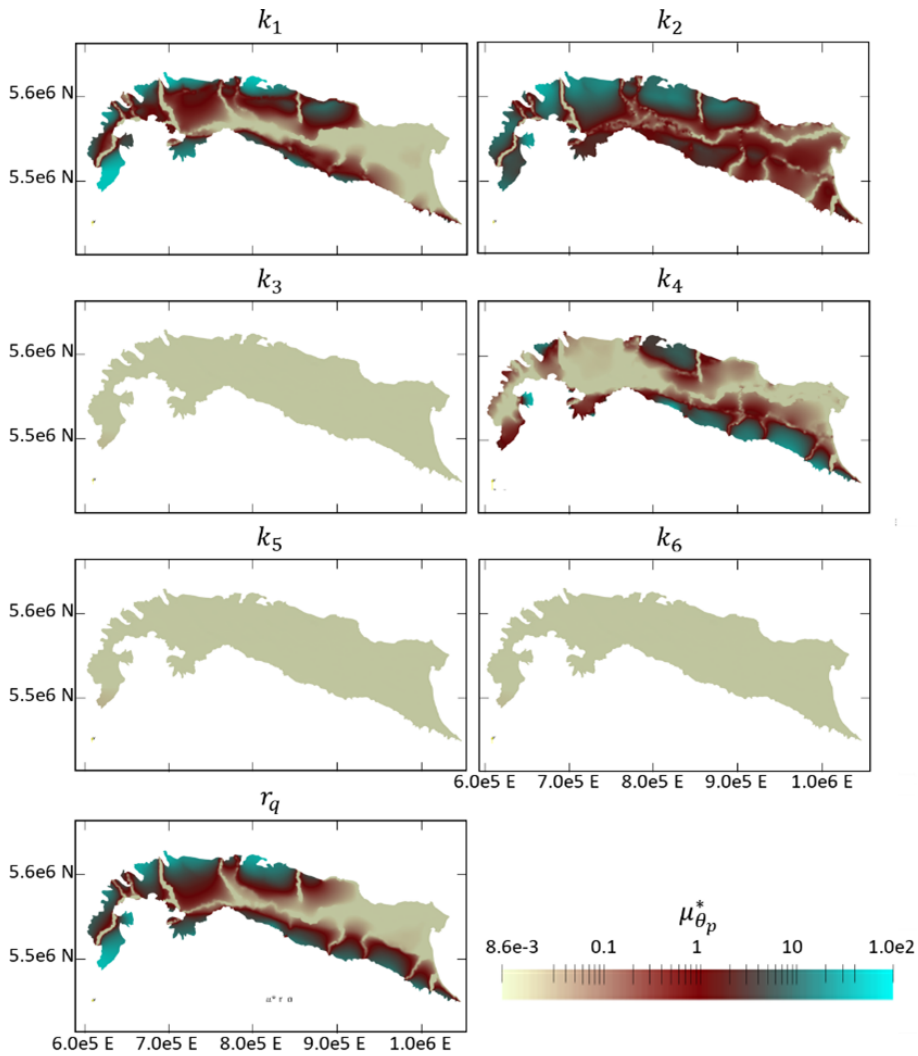

Figure 11. Spatial distribution of Morris indices related to geomaterial permeabilities (k_1,... , k_6) and correction coefficient, r_q, across the top layer of the model.

ary conditions (see Sect. 4.2), thus shadowing the effect of river–groundwater exchanges.

In Italy, irrigation channels have been documented to operate with efficiencies ranging from 0.43 to 0.6 (Wriedt et al., 2009). Then, a significant amount of the water lost from these channels enters the groundwater system. In this context, channels and rivers such as the Naviglio Grande and the Lambro (associated with α_{19} and α_{20}, respectively) show a significant influence on the local hydraulic head distribution, even as they are characterized by a generally low flow rate. This is related to the observation that they are located in an area with a dense irrigation channel network (De Caro et al., 2020) and their contribution to groundwater flow includes the cumulative effect of a high number of small irrigation channels. Figure S1 (see the Supplement) illustrates the portions of the rivers which recharge or drain the aquifer.

It is worth noting that all Morris indices display only modest variability along the vertical direction. The complete three-dimensional spatial distribution of $\mu^*_{\theta_p}$ and a grid containing 10 cross sections highlighting our findings about the vertical variability in Morris indices can be accessed in an open-source Visualization Toolkit (VTK) format for structured grids (Schroeder et al., 2006). These data are available on a code and data repository (https://doi.org/10.5281/zenodo.10664413, Manzoni, 2024).

5 Conclusions

The study introduces a comprehensive methodology that combines advanced numerical and data analysis methods, such as multi-objective optimization, informed GSA, and three-dimensional groundwater modeling, to analyze subsurface flow dynamics across large-scale domains. We support

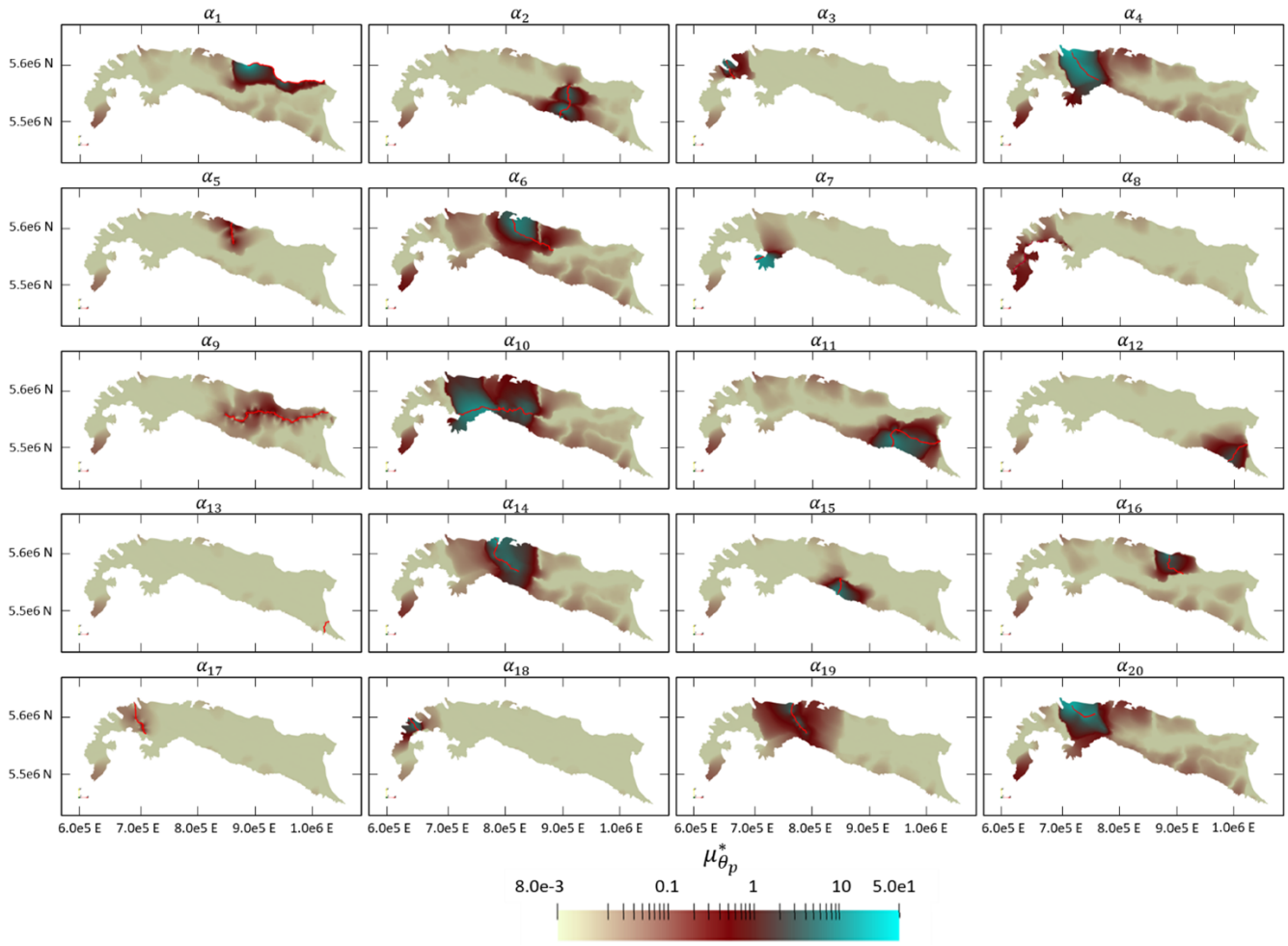

Figure 12. Spatial distribution (across the top layer of the model) of Morris indices related to specific conductance of the riverbeds.

the suitability of the proposed approach to assess large-scale complex groundwater systems by employing it to analyze the main features of Italy's largest groundwater system, which is set within the Po River watershed. Our work leads to the following major conclusions.

Groundwater recharge is evaluated across the analyzed large-scale system, relying jointly on remote sensing information and on-site data on land use and soil properties. While our results are overall consistent with prior findings across the area based on a global water balance approach (Rossi et al., 2022), they are also associated with an enhanced spatial resolution. As such, they provide the basis for future applications aimed at delineating areas associated with vulnerability of the groundwater resource.

A coevolutionary algorithm is successfully employed for the calibration of our large-scale groundwater system model. Our approach allows for differentiating the use of data depending on the spatial location of the observation wells. Notably, our approach is tailored to separate calibration of riverbed conductance, thus addressing surface–groundwater interactions with a dedicated optimization. Casting model calibration within a stochastic context yields quantification of the residual (i.e., after calibration on available information) uncertainty associated with model parameters. This ultimately enables one to identify model parameters whose estimates are associated with large uncertainty (as rendered through estimation variance) on the basis of the available dataset. In our scenario, the resulting model parameterization enables us to subdivide the domain into three macro-areas, each characterized by mild spatial heterogeneity of permeability. The spatial arrangement of these areas is in line with the distribution of sediment types documented by available geological maps associated with the studied domain (Compagnoni et al., 2004). While relying on a characterization of the system through a block-heterogeneous conceptual picture is consistent with the scale tackled in our study, a detailed assessment of heterogeneous conductivity patterns might be required when targeting local-scale settings. The latter can then be nested in the context of the large-scale patterns documented in our study.

The calibrated model enables us to identify three-dimensional flow patterns, as driven by the (three-dimensional) heterogeneous distribution of geomaterials across the subsurface. This represents a significant advancement as compared to commonly developed large-scale models based on 2D geological maps.

A global sensitivity analysis (GSA) quantifies the relative importance of uncertain model parameters on a target model output (i.e., hydraulic heads) across the whole domain. Our results document the spatially heterogeneous distribution of global sensitivity metrics associated with model parameters, thus providing information about where the acquisition of future information could contribute to enhancing the quality of groundwater flow model parameterization and constraining hydraulic head estimates. Our findings suggest that the features of the foothills (an area that is highly unexplored to date as compared to lowland areas) should be subject to additional investigation to improve the quality of hydraulic head estimates. Furthermore, GSA results allow for identifying rivers where information on water exchange with groundwater could be beneficial to improve piezometric characterization.

Code and data availability. All data and codes are available on the following repositories: https://doi.org/10.5281/zenodo.10664413 (Manzoni, 2024) and https://doi.org/10.5281/zenodo.10013442 (Manzoni, 2023).

Supplement. The supplement related to this article is available online at: https://doi.org/10.5194/hess-28-2661-2024-supplement.

Author contributions. AM, GMP, LG, AG, and MR: conceptualization; AM: data curation; AM, GMP, LG, AG, and MR: formal analysis; AG and MR: funding acquisition; AM, GMP, LG, AG, and MR: methodology; GMP, AG, and MR: project administration; AM: software; GMP, LG, AG, and MR: supervision; AM, GMP, LG, AG, and MR: validation; AM, GMP, LG, AG, and MR: visualization; AM, GMP, LG, AG, and MR: writing (original draft preparation); AM, GMP, LG, AG, and MR: writing (review and editing).

Competing interests. At least one of the (co-)authors is a member of the editorial board of *Hydrology and Earth System Sciences*. The peer-review process was guided by an independent editor, and the authors also have no other competing interests to declare.

Disclaimer. Publisher's note: Copernicus Publications remains neutral with regard to jurisdictional claims made in the text, published maps, institutional affiliations, or any other geographical representation in this paper. While Copernicus Publications makes every effort to include appropriate place names, the final responsibility lies with the authors.

Financial support. Monica Riva has been funded under the National Recovery and Resilience Plan (NRRP), mission 4 component 2 investment 1.4 – call for tender no. 3138 of 16 December 2021, rectified by decree no. 3175 of 18 December 2021 of Italian Ministry of University and Research funded by the European Union – NextGenerationEU, project code CN_00000033, concession decree no. 1034 of 17 June 2022 adopted by the Italian Ministry of University and Research, CUP D43C22001250001, project title "National Biodiversity Future Center – NBFC". Support from Water Alliance (Acque di Lombardia) was also received. Andrea Manzoni and Alberto Guadagnini have been supported by the European Union's Horizon 2020 research and innovation program under the Marie Skłodowska-Curie program (grant agreement no. 872607) in the context of the coordinated research program RECYCLE. Giovanni Michele Porta has been supported by the NRRP Next Generation EU Investment 1.1 through the PRIN "Uncertainty Quantification of coupled models for water flow and contaminant transport" project.

Review statement. This paper was edited by Ralf Loritz and reviewed by two anonymous referees.

References

AdB-Po: Piano di Gestione del distretto idrografico del fiume Po al 2021, https://www.adbpo.it/PianoAcque2021/PdGPo2021_22dic21/, 2021 (in Italian).

Agenzia Regionale per la Protezione Ambientale Piemonte: Portale acque, Agenzia Regionale per la Protezione Ambientale Piemonte [data set], https://www.arpa.piemonte.it/rischinaturali/accesso-ai-dati, 2020 (in Italian).

Agrawala, S.: Climate change in the European Alps: adapting winter tourism and natural hazards management, OECD (Organisation for Economic Co-operation and Development, https://doi.org/10.1787/9789264031692-en, 2007.

Allen, R. G., Pereira, L. S., Raes, D., and Smith, M.: Crop evapotranspiration: Guidelines for computing crop water requirements, FAO Irrigation and Drainage Paper No. 56, Food and Agriculture Organization of the United Nations, ISBN 92-5-104219-5, 1998.

Amanambu, A. C., Obarein, O. A., Mossa, J., Li, L., Ayeni, S. S., Balogun, O., Oyebamiji, A., and Ochege, F. U.: Groundwater system and climate change: Present status and future considerations, J. Hydrol., 589, 125163, https://doi.org/10.1016/j.jhydrol.2020.125163, 2020.

Antonellini, M., Mollema, P., Giambastiani, B., Bishop, K., Caruso, L., Minchio, A., Pellegrini, L., Sabia, M., Ulazzi, E., and Gabbianelli, G.: Salt water intrusion in the coastal aquifer of the southern Po Plain, Italy, Hydrogeol. J., 16, 1541–1556, https://doi.org/10.1007/s10040-008-0319-9, 2008.

Balestrini, R., Delconte, C. A., Sacchi, E., and Buffagni, A.: Groundwater-dependent ecosystems as transfer vectors of nitrogen from the aquifer to surface waters in agricultural basins: The fontanili of the Po Plain (Italy), Sci. Total Environ., 753, 141995, https://doi.org/10.1016/j.scitotenv.2020.141995, 2021.

Bianchi Janetti, E., Guadagnini, L., Riva, M., and Guadagnini, A.: Global sensitivity analyses of multiple conceptual models with uncertain parameters driving groundwater flow in a

regional-scale sedimentary aquifer, J. Hydrol., 574, 544–556, https://doi.org/10.1016/j.jhydrol.2019.04.035, 2019.

Bianchi Janetti, E., Riva, M., and Guadagnini, A.: Natural springs protection and probabilistic risk assessment under uncertain conditions, Sci. Total Environ., 751, 141430, https://doi.org/10.1016/j.scitotenv.2020.141430, 2021.

Bilke, L., Fischer, T., Naumov, D., Lehmann, C., Wang, W., Lu, R., Meng, B., Rink, K., Grunwald, N., Buchwald, J., Silbermann, C., Habel, R., Günther, L., Mollaali, M., Meisel, T., Randow, J., Einspänner, S., Shao, H., Kurgyis, K., Kolditz, O., and Garibay, J.: OpenGeoSys, Version 6.4.3, Zenodo [code], https://doi.org/10.5281/zenodo.7092676, 2022.

Bonafè, G., Morgillo, A., and Minguzzi, E.: Weather types and wind patterns classification in the Po Valley, during the PEGASOS field campaign (summer 2012), in: EGU General Assembly Conference Abstracts, p. 11939, 2014.

Bozzola, M. and Swanson, T.: Policy implications of climate variability on agriculture: Water management in the Po river basin, Italy, Environ. Sci. Policy, 43, 26–38, https://doi.org/10.1016/j.envsci.2013.12.002, 2014.

Campolongo, F., Cariboni, J., and Saltelli, A.: An effective screening design for sensitivity analysis of large models, Environ. Modell. Softw., 22, 1509–1518, https://doi.org/10.1016/j.envsoft.2006.10.004, 2007.

Carcano, C. and Piccin, A.: Geologia degli acquiferi Padani della Regione Lombardia Regione Lombardia, Eni Divisione Agip, https://www.cartografia.regione.lombardia.it/metadata/acquiferi/doc/ (last access: 1 October 2022), 2001.

Carrera, J. and Neuman, S. P.: Estimation of Aquifer Parameters Under Transient and Steady State Conditions: 1. Maximum Likelihood Method Incorporating Prior Information, Water Resour. Res., 22, 199–210, https://doi.org/10.1029/WR022i002p00199, 1986.

Colombani, N., Volta, G., Osti, A., and Mastrocicco, M.: Misleading reconstruction of seawater intrusion via integral depth sampling, J. Hydrol., 536, 320–326, https://doi.org/10.1016/j.jhydrol.2016.03.011, 2016.

Compagnoni, B., Galluzzo, F., Bonomo, R., Capotorti, F., D'Ambrogi, C., Di Stefano, R., Graziano, R., Martarelli, L., Pampaloni, M. L., Pantaloni, M., Ricci, V., Tacchia, D., Masella, G., Pannuti, V., Ventura, R., and Vitale, V.: Carta Geologica d'Italia, in: 32° CGI, 2004.

Dagdia, Z. C. and Mirchev, M.: When Evolutionary Computing Meets Astro- and Geoinformatics, in: Knowledge Discovery in Big Data from Astronomy and Earth Observation, edited by: Škoda, P. and Adam, F., Elsevier, 283–306, https://doi.org/10.1016/B978-0-12-819154-5.00026-6, 2020.

d'Andrimont, R., Verhegghen, A., Lemoine, G., Kempeneers, P., Meroni, M., and van der Velde, M.: From parcel to continental scale – A first European crop type map based on Sentinel-1 and LUCAS Copernicus in-situ observations, Remote Sens. Environ., 266, 112708, https://doi.org/10.1016/j.rse.2021.112708, 2021.

De Caro, M., Perico, R., Crosta, G. B., Frattini, P., and Volpi, G.: A regional-scale conceptual and numerical groundwater flow model in fluvio-glacial sediments for the Milan Metropolitan area (Northern Italy), Journal of Hydrology: Regional Studies, 29, 100683, https://doi.org/10.1016/j.ejrh.2020.100683, 2020.

de Graaf, I., Condon, L., and Maxwell, R.: Hyper-Resolution Continental-Scale 3-D Aquifer Parameterization for Groundwater Modeling, Water Resour. Res., 56, e2019WR026004, https://doi.org/10.1029/2019WR026004, 2020.

De Lange, W. J., Prinsen, G. F., Hoogewoud, J. C., Veldhuizen, A. A., Verkaik, J., Oude Essink, G. H. P., Van Walsum, P. E. V., Delsman, J. R., Hunink, J. C., Massop, H. T. L., and Kroon, T.: An operational, multi-scale, multi-model system for consensus-based, integrated water management and policy analysis: The Netherlands Hydrological Instrument, Environ. Modell. Softw., 59, 98–108, https://doi.org/10.1016/j.envsoft.2014.05.009, 2014.

Dell'Oca, A., Riva, M., and Guadagnini, A.: Moment-based metrics for global sensitivity analysis of hydrological systems, Hydrol. Earth Syst. Sci., 21, 6219–6234, https://doi.org/10.5194/hess-21-6219-2017, 2017.

Dell'Oca, A., Riva, M., and Guadagnini, A.: Global Sensitivity Analysis for Multiple Interpretive Models With Uncertain Parameters, Water Resour. Res., 56, e2019WR025754, https://doi.org/10.1029/2019WR025754, 2020.

Dell'Oca, A., Manzoni, A., Siena, M., Bona, N. G., Moghadasi, L., Miarelli, M., Renna, D., and Guadagnini, A.: Stochastic inverse modeling of transient laboratory-scale three-dimensional two-phase core flooding scenarios, Int. J. Heat Mass. Tran., 202, 123716, https://doi.org/10.1016/j.ijheatmasstransfer.2022.123716, 2023.

Dripps, W. R. and Bradbury, K. R.: A simple daily soil-water balance model for estimating the spatial and temporal distribution of groundwater recharge in temperate humid areas, Hydrogeol. J., 15, 433–444, https://doi.org/10.1007/s10040-007-0160-6, 2007.

Elsasser, H. and Bürki, R.: Climate change as a threat to tourism in the Alps, Clim. Res., 20, 253–257, https://doi.org/10.3354/cr020253, 2002.

ESA: Copernicus DEM, ESA [data set], https://doi.org/10.5270/ESA-c5d3d65, 2019.

Éupolis Lombardia: Piano di Tutela delle Aque - revisione dei corpi idrici lombardia, 2016.

European Environment Agency (EEA): CORINE Land Cover 2018, EEA [data set], https://doi.org/10.2909/71c95a07-e296-44fc-b22b-415f42acfdf0, 2018.

Farinotti, D., Pistocchi, A., and Huss, M.: From dwindling ice to headwater lakes: Could dams replace glaciers in the European Alps?, Environ. Res. Lett., 11, 054022, https://doi.org/10.1088/1748-9326/11/5/054022, 2016.

Fratianni, S. and Acquaotta, F.: The Climate of Italy, Landscapes and Landforms of Italy, Springer International Publishing, 29–38, https://doi.org/10.1007/978-3-319-26194-2_4, 2017.

Geuzaine, C. and Remacle, J.-F.: Gmsh: A 3-D finite element mesh generator with built-in pre- and post-processing facilities, Int. J. Numer. Meth. Eng., 79, 1309–1331, https://doi.org/10.1002/nme.2579, 2009.

Giuliano, G.: Ground water in the PO basin: some problems relating to its use and protection, Sci. Total Environ., 171, 17–27, 1995.

Grimm, M., Jones, R. J. A., Rusco, E., and Montanarella, L.: Soil Erosion Risk in Italy: a revised USLE approach, European Soil Bureau Research Report No. 11, EUR 20677 EN, 28 pp., Office for Official Publications of the European Communities, Luxembourg, 2023.

Guadagnini, L., Menafoglio, A., Sanchez-Vila, X., and Guadagnini, A.: Probabilistic assessment of spatial heterogeneity of natural background concentrations in large-scale groundwater bod-

ies through Functional Geostatistics, Sci. Total Environ., 740, 140139, https://doi.org/10.1016/j.scitotenv.2020.140139, 2020.

Hargreaves, G. H. and Samani, Z. A.: Reference Crop Evapotranspiration from Temperature, Appl. Eng. Agric., 1, 96–99, https://doi.org/10.13031/2013.26773, 1985.

Hendricks Franssen, H. J., Alcolea, A., Riva, M., Bakr, M., van der Wiel, N., Stauffer, F., and Guadagnini, A.: A comparison of seven methods for the inverse modelling of groundwater flow. Application to the characterisation of well catchments, Adv. Water Resour., 32, 851–872, https://doi.org/10.1016/j.advwatres.2009.02.011, 2009.

Højberg, A. L., Troldborg, L., Stisen, S., Christensen, B. B. S., and Henriksen, H. J.: Stakeholder driven update and improvement of a national water resources model, Environ. Modell. Softw., 40, 202–213, https://doi.org/10.1016/j.envsoft.2012.09.010, 2013.

ISPRA: Reticolo Idrografico Nazionale, ISPRA [data set], https://geodati.gov.it/resource/id/ispra_rm:01Idro250N_DT (last access: 1 October 2022), 2010.

ISTAT: Public water supply use, ISTAT [data set], http://dati.istat.it/, 2020.

Kazakis, N., Busico, G., Colombani, N., Mastrocicco, M., Pavlou, A., and Voudouris, K.: GALDIT-SUSI a modified method to account for surface water bodies in the assessment of aquifer vulnerability to seawater intrusion, J. Environ. Manage., 235, 257–265, https://doi.org/10.1016/j.jenvman.2019.01.069, 2019.

Khan, S., Grudniewski, P., Muhammad, Y. S., and Sobey, A. J.: The benefits of co-evolutionary Genetic Algorithms in voyage optimisation, Ocean Eng., 245, 110261, https://doi.org/10.1016/j.oceaneng.2021.110261, 2022.

Kim, K. B., Kwon, H.-H., and Han, D.: Exploration of warm-up period in conceptual hydrological modelling, J. Hydrol., 556, 194–210, https://doi.org/10.1016/j.jhydrol.2017.11.015, 2018.

Manzoni, A.: manzoniandrea/Large_Basin_Scale_Recarge_Rate: Large_Basin_Scale_Recarge_Ratev1.0.0, Version Large_Basin_Scale_Recarge_Ratev1.0.0, Zenodo [code], https://doi.org/10.5281/zenodo.10013442, 2023.

Manzoni, A.: manzoniandrea/Large-scaleGWFlow: largeScale, Version v1.0.6, Zenodo [code], https://doi.org/10.5281/zenodo.10664413, 2024.

Manzoni, A., Porta, G. M., Guadagnini, L., Guadagnini, A., and Riva, M.: Probabilistic reconstruction via machine-learning of the Po watershed aquifer system (Italy), Hydrogeol. J., 31, 1547–1563, https://doi.org/10.1007/s10040-023-02677-8, 2023.

Mather, B., Müller, R. D., O'Neill, C., Beall, A., Vervoort, R. W., and Moresi, L.: Constraining the response of continental-scale groundwater flow to climate change, Sci. Rep.-UK, 12, 4539, https://doi.org/10.1038/s41598-022-08384-w, 2022.

Maxwell, R. M., Condon, L. E., and Kollet, S. J.: A high-resolution simulation of groundwater and surface water over most of the continental US with the integrated hydrologic model ParFlow v3, Geosci. Model Dev., 8, 923–937, https://doi.org/10.5194/gmd-8-923-2015, 2015.

Mishra, S. K. and Singh, V. P.: Soil Conservation Service Curve Number (SCS-CN) Methodology, Springer Science & Business Media, https://doi.org/10.1007/978-94-017-0147-1, 2003.

Molnau, M. and Bissell, V.: A continuous frozen ground index for flood forecasting, in: Proceedings 51st Annual Meeting Western Snow Conference, Vancouver, 19–21 April 1983, 109–119, 1983.

Morgan Jr., G. M.: A General Description of the Hail Problem in the Po Valley of Northern Italy, J. Appl. Meteorol., 12, 338–353, https://doi.org/10.1175/1520-0450(1973)012<0338:AGDOTH>2.0.CO;2, 1973.

Morris, M. D.: Factorial Sampling Plans for Preliminary Computational Experiments, Technometrics, 33, 161–174, https://doi.org/10.2307/1269043, 1991.

Muñoz-Sabater, J., Dutra, E., Agustí-Panareda, A., Albergel, C., Arduini, G., Balsamo, G., Boussetta, S., Choulga, M., Harrigan, S., Hersbach, H., Martens, B., Miralles, D. G., Piles, M., Rodríguez-Fernández, N. J., Zsoter, E., Buontempo, C., and Thépaut, J.-N.: ERA5-Land: a state-of-the-art global reanalysis dataset for land applications, Earth Syst. Sci. Data, 13, 4349–4383, https://doi.org/10.5194/essd-13-4349-2021, 2021.

Naz, B. S., Sharples, W., Ma, Y., Goergen, K., and Kollet, S.: Continental-scale evaluation of a fully distributed coupled land surface and groundwater model, ParFlow-CLM (v3.6.0), over Europe, Geosci. Model Dev., 16, 1617–1639, https://doi.org/10.5194/gmd-16-1617-202, 2023.

Nespoli, M., Cenni, N., Belardinelli, M. E., and Marcaccio, M.: The interaction between displacements and water level changes due to natural and anthropogenic effects in the Po Plain (Italy): The different point of view of GNSS and piezometers, J. Hydrol., 596, 126112, https://doi.org/10.1016/j.jhydrol.2021.126112, 2021.

Neuman, S. P.: Maximum likelihood Bayesian averaging of uncertain model predictions, Stoch. Env. Res. Risk A., 17, 291–305, https://doi.org/10.1007/s00477-003-0151-7, 2003.

OpenStreetMap: OpenStreetMap database [PostgreSQL], OpenStreetMap Foundation, Cambridge, UK, https://gisdata.mapog.com/italy/Municipality%20level%204 (last access: 1 October 2022), 2021.

Panzeri, M., Riva, M., Guadagnini, A., and Neuman, S. P.: EnKF coupled with groundwater flow moment equations applied to Lauswiesen aquifer, Germany, J. Hydrol., 521, 205–216, https://doi.org/10.1016/j.jhydrol.2014.11.057, 2015.

Pianosi, F., Beven, K., Freer, J., Hall, J. W., Rougier, J., Stephenson, D. B., and Wagener, T.: Sensitivity analysis of environmental models: A systematic review with practical workflow, Environ. Modell. Softw., 79, 214–232, https://doi.org/10.1016/j.envsoft.2016.02.008, 1 May 2016.

Poggio, L., de Sousa, L. M., Batjes, N. H., Heuvelink, G. B. M., Kempen, B., Ribeiro, E., and Rossiter, D.: SoilGrids 2.0: producing soil information for the globe with quantified spatial uncertainty, SOIL, 7, 217–240, https://doi.org/10.5194/soil-7-217-2021, 2021.

Razavi, S. and Gupta, H. V.: What do we mean by sensitivity analysis? The need for comprehensive characterization of "global" sensitivity in Earth and Environmental systems models, Water Resour. Res., 51, 3070–3092, https://doi.org/10.1002/2014WR016527, 2015.

Regione Emilia-Romagna and ENI-AGIP: Riserve idriche sotterranee della Regione Emilia-Romagna. S.EL.CA, Firenze, 1998 (in Italian).

Regione Emilia-Romagna: Piezometrie e qualità delle acque sotterranee nella pianura emiliano-romagnola, Regione Emilia-Romagna [data set], https://ambiente.regione.emilia-romagna.it/it/geologia/cartografia/webgis-banchedati/

piezometrie-qualita-acque-sotterranee (last access: 1 October 2022), 2020.

Regione Emilia-Romagna: Riserve idriche sotterranee della Regione Emilia-Romagna, 1998 (in Italian).

Regione Lombardia: Banca dati geologica sottosuolo, Regione Lombardia [data set], https://www.geoportale.regione.lombardia.it/metadati?p_p_id=detailSheetMetadata_WAR_gptmetadataportlet&p_p_lifecycle=0&p_p_state=normal&p_p_mode=view&_detailSheetMetadata_WAR_gptmetadataportlet_identifier=r_lombar%3Aad085d2a-519f-4ed6-a84f-b81de6cec1db&_jsfBridgeRedirect=true (last access: 1 August 2022), 2016.

Regione Lombardia and ENI-AGIP: Geologia degli acquiferi padani della Regione Lombardia. S.EL.CA, Firenze, 2002 (in Italian).

Regione Lombardia: Geoportale della Lombardia, Regione Lombardia [data set], https://www.geoportale.regione.lombardia.it/ (last access: 1 March 2022), 2021.

Regione Piemonte: Geoportale Piemonte, Regione Piemonte [data set], https://www.geoportale.piemonte.it/geonetwork/srv/eng/catalog.search#/metadata/r_piemon:023ef6df-b781-4751-b5d2-a442427916d0 (last access: 1 June 2022), 2022.

Ricci Lucchi, F., Colalongo, M. L., Cremonini, G., Gasperi, G. F., Iaccarino, S., Papani, G., Raffi, S., and Rio, D.: Evoluzione sedimentaria e paleogeografica del margine appenninico (Sedimentary and palaeogeographic evolution of the Apenninic margin), Guida alla geologia del margine appenninico padano, Guide geologiche regionali, Soc. Geol. Ital., 17–46, 1982.

Rink, K., Bilke, L., and Kolditz, O.: Visualisation Strategies for Modelling and Simulation Using Geoscientific Data, in: 1st Workshop on Visualisation in Environmental Sciences (EnvirVis), EuroVis 2013, Leipzig, Germany, 17–18 June 2013, The Eurographics Association, 47–51, https://doi.org/10.2312/PE.EnvirVis.EnvirVis13.047-051, 2013.

Riva, M., Guadagnini, A., Neuman, S. P., Janetti, E. B., and Malama, B.: Inverse analysis of stochastic moment equations for transient flow in randomly heterogeneous media, Adv. Water Resour., 32, 1495–1507, https://doi.org/10.1016/j.advwatres.2009.07.003, 2009.

Roland, C. J., Zoet, L. K., Rawling, J. E., and Cardiff, M.: Seasonality in cold coast bluff erosion processes, Geomorphology, 374, 107520, https://doi.org/10.1016/j.geomorph.2020.107520, 2021.

Rossi, M., Donnini, M., and Beddini, G.: Nationwide groundwater recharge evaluation for a sustainable water withdrawal over Italy, Journal of Hydrology: Regional Studies, 43, 101172, https://doi.org/10.1016/j.ejrh.2022.101172, 2022.

Schaap, M. G., Leij, F. J., and van Genuchten, M. T.: ROSETTA: a computer program for estimating soil hydraulic parameters with hierarchical pedotransfer functions, J. Hydrol., 251, 163–176, https://doi.org/10.1016/S0022-1694(01)00466-8, 2001.

Schroeder, W., Martin, K., and Lorensen, B.: The Visualization Toolkit, 4th edn., edited by: Squillacote, A., Kitware, 528 pp., ISBN-10: 193093419X, ISBN-13: 978-1930934191, 2006.

SEDAC: Gridded Population of the World (GPWv4), Version 4: Population Density, Revision 11, SEDAC [data set], https://doi.org/10.7927/H49C6VHW, 2018.

Shrestha, P., Sulis, M., Masbou, M., Kollet, S., and Simmer, C.: A scale-consistent terrestrial systems modeling platform based on COSMO, CLM, and ParFlow, Mon. Weather Rev., 142, 3466–3483, https://doi.org/10.1175/MWR-D-14-00029.1, 2014.

Shuler, C., Brewington, L., and El-Kadi, A. I.: A participatory approach to assessing groundwater recharge under future climate and land-cover scenarios, Tutuila, American Samoa, Journal of Hydrology: Regional Studies, 34, 100785, https://doi.org/10.1016/j.ejrh.2021.100785, 2021.

Siena, M. and Riva, M.: Impact of geostatistical reconstruction approaches on model calibration for flow in highly heterogeneous aquifers, Stoch. Env. Res. Risk A., 34, 1591–1606, https://doi.org/10.1007/s00477-020-01865-2, 2020.

Simoncini, D. and Zhang, K. Y. J.: Population-Based Sampling and Fragment-Based De Novo Protein Structure Prediction, in: Encyclopedia of Bioinformatics and Computational Biology, edited by: Ranganathan, S., Gribskov, M., Nakai, K., and Schönbach, C., Elsevier, 774–784, https://doi.org/10.1016/B978-0-12-809633-8.20507-4, 2019.

Soltani, S. S., Fahs, M., Bitar, A. A., and Ataie-Ashtiani, B.: Improvement of soil moisture and groundwater level estimations using a scale-consistent river parameterization for the coupled ParFlow-CLM hydrological model: A case study of the Upper Rhine Basin, J. Hydrol., 610, 127991, https://doi.org/10.1016/j.jhydrol.2022.127991, 2022.

Sophocleous, M. and Perkins, S. P.: Methodology and application of combined watershed and ground-water models in Kansas, J. Hydrol., 236, 185–201, https://doi.org/10.1016/S0022-1694(00)00293-6, 2000.

Storn, R. and Price, K.: A Simple and Efficient Heuristic for Global Optimization over Continuous Spaces, J. Global Optim., 11, 341–359, https://doi.org/10.1023/A:1008202821328, 1997.

Thornthwaite, C. W.: An Approach toward a Rational Classification of Climate, Geogr. Rev., 38, 55–94, https://doi.org/10.2307/210739, 1948.

Thornthwaite, C. W. and Mather, J. R.: The water balance, Publications in Climatology, Drexel Institute of Technology, Laboratory of Climatology, 1955.

Thornthwaite, C. W. and Matter, J. R.: Instructions and Tables for Computing Potential Evaporation and the Water Balance, Climatology, Drexel Institute of Technology, Laboratory of Climatology, 1957.

Trunfio, G. A.: A Cooperative Coevolutionary Differential Evolution Algorithm with Adaptive Subcomponents, Procedia Comput. Sci., 51, 834–844, https://doi.org/10.1016/j.procs.2015.05.209, 2015.

Tusar, T. and Filipic, B.: Differential evolution versus genetic algorithms in multiobjective optimization, Evolutionary Multi-Criterion Optimization, Springer Berlin Heidelberg, 257–271, https://doi.org/10.1007/978-3-540-70928-2_22, 2007.

Vrugt, J. A., Stauffer, P. H., Wöhling, Th., Robinson, B. A., and Vesselinov, V. V.: Inverse Modeling of Subsurface Flow and Transport Properties: A Review with New Developments, Vadose Zone J., 7, 843–864, https://doi.org/10.2136/vzj2007.0078, 2008.

Westenbroek, S. M., Engott, J. A., Kelson, V. A., and Hunt, R. J.: SWB Version 2.0 – A soil-water-balance code for estimating net infiltration and other water-budget components, U.S. Geological Survey, Techniques and Methods 6–A59, https://doi.org/10.3133/tm6A59, 2018.

Wriedt, G., Van der Velde, M., Aloe, A., and Bouraoui, F.: Estimating irrigation water requirements in Europe, J. Hydrol., 373, 527–544, https://doi.org/10.1016/j.jhydrol.2009.05.018, 2009.

Yang, Z., Tang, K., and Yao X.: Large scale evolutionary optimization using cooperative coevolution, Inform. Sciences, 178, 2985–2999, https://doi.org/10.1016/j.ins.2008.02.017, 2008.

Ye, M., Pohlmann, K. F., Chapman, J. B., Pohll, G. M., and Reeves, D. M.: A model-averaging method for assessing groundwater conceptual model uncertainty, Ground Water, 48, 716–728, https://doi.org/10.1111/j.1745-6584.2009.00633.x, 2010.

Zhang, J., Felzer, B. S., and Troy, T. J.: Extreme precipitation drives groundwater recharge: the Northern High Plains Aquifer, central United States, 1950–2010, Hydrol. Process., 30, 2533–2545, https://doi.org/10.1002/hyp.10809, 2016.

Zhou, H., Gómez-Hernández, J. J., and Li, L.: Inverse methods in hydrogeology: Evolution and recent trends, Adv. Water Resour., 63, 22–37, https://doi.org/10.1016/j.advwatres.2013.10.014, 2014.

Zhou, Y. and Li, W.: A review of regional groundwater flow modeling, Geosci. Front., 2, 205–214, https://doi.org/10.1016/j.gsf.2011.03.003, 2011.